

Title: First Principles Design of a Single-Atom Alloy Propane Dehydrogenation Catalyst

Authors: Ryan T. Hannagan^{1†}, Georgios Giannakakis^{2†}, Romain Réocreux^{3†}, Julia Schumann^{3,4,5}, Jordan Finzel⁶, Yicheng Wang¹, Angelos Michaelides^{4,5}, Prashant Deshlahra², Philip Christopher⁶, Maria Flytzani-Stephanopoulos², Michail Stamatakis^{3*}, E. Charles H. Sykes^{1*}

Affiliations:

¹Department of Chemistry, Tufts University, Medford, MA 02155, United States.

²Department of Chemical and Biological Engineering, Tufts University, Medford, MA 02155, United States.

³Thomas Young Centre and Department of Chemical Engineering, University College London, Roberts Building, Torrington Place, London WC1E 7JE, United Kingdom.

⁴Yusuf Hamied Department of Chemistry, University of Cambridge, Lensfield Road, CB2 1EW Cambridge, United Kingdom.

⁵Department of Physics and Astronomy, University College London, Gower Street, London WC1E 6BT, United Kingdom.

⁶Department of Chemical Engineering, University of California, Santa Barbara, CA 93106, United States.

*Correspondence to: m.stamatakis@ucl.ac.uk and charles.sykes@tufts.edu

†These authors contributed equally to the work

Abstract: The complexity of heterogeneous catalysts means a priori design of new catalytic materials is difficult, but the well-defined nature of single-atom alloy catalysts has made unambiguous modelling with theory and surface science feasible. Herein we report the theory-led discovery of a RhCu single-atom alloy catalyst for propane dehydrogenation to propene. Although Rh is not generally considered for alkane dehydrogenation, first-principles calculations revealed that Rh atoms disperse in Cu and exhibit low alkane C-H activation barriers. Surface science experiments confirmed these predictions, and together, these results informed the design of a highly active, selective and coke resistant RhCu nanoparticle catalyst that enables low-temperature non-oxidative propane dehydrogenation.

One Sentence Summary: Isolated Rh atoms in Cu enable facile C-H activation and coke-free propane dehydrogenation.

Main Text: Despite their widespread prevalence in industry, the improvement of heterogeneous catalysts is usually an empirical process, and examples of rational design remain extremely rare (see e.g. (1, 2)). Rational design is impeded in part by the enormous complexity of most heterogeneous catalysts, which often consist of metal nanoparticles (NPs) that expose a wide range of active sites with which the reactants can interact and react (3). Metal NPs can also restructure under reaction conditions (4). One approach to reduce the complexity of metal NPs is to reduce the active site to a single atom (5, 6). However, the heterogeneity of the oxide support and the

adaptive nature of the local environment make rational design of even these materials challenging (7, 8).

Single-atom alloys (SAAs), a sub-class of single-atom catalysts, are comprised of a reactive dopant metal atomically dispersed in a second metal host (9). Many SAAs are active, selective, and robust for a wide variety of reactions because the thermodynamics of mixing favor the atomic dispersion of the dopant in the more inert but more selective host (10). Furthermore, the well-defined nature of the active sites in SAAs, which have been atomically resolved in both model and NP systems makes unambiguous modelling of their behavior with theory possible (11–13).

Guided by theoretical predictions, we present the rational design of a RhCu SAA catalyst for non-oxidative propane dehydrogenation to two valuable compounds, propene and hydrogen (14). Our theoretical screening of SAA combinations for this reaction began by examining C-H activation of methane, which is the simplest probe molecule for establishing trends in C-H activation. Using density functional theory (DFT) we determined (i) the activation energy of the first C-H scission, and (ii) the segregation energy, which reflects the propensity of the dopant atom to migrate from the surface layer to the bulk of the host metal (see computational details in SM). Of all the SAA combinations screened, the Rh doped alloys have the lowest C-H activation energies (Fig. 1A, S1, S2, and S3). In fact, these C-H activation energies are similar to pure transition metals (Pt and Rh) and the industrially relevant Pt₃Sn(111) (2×2) intermetallic (see Fig. 1 and S3) (15). However, of the three Rh doped SAAs, RhCu(111) has the most favorable mixing enthalpy and segregation energy when reaction intermediates are present (see Fig. 1A, S1, S2, and ref. (16)). Specific to the mixing enthalpy, the energy change for isolated Rh atoms in a Cu(111) surface to form a dimer or a trimer is positive (>0.16 eV), indicating that the thermodynamic stability of single Rh atoms is greater than that of Rh clusters in a Cu host making it a promising SAA catalyst (16).

Comparison of the geometric and electronic structures of adsorbed methane on the SAA provided insight into the magnitude of the C-H activation barriers (Fig. 1B and S4). On the RhCu(111) SAA surface, methane adsorbed 0.35 Å closer to the dopant atom than on pure Cu(111) (see Table S1 and S2). This shorter distance increased the charge density difference $\Delta\rho(\mathbf{r})$ upon adsorption (see Fig. 1B and S4) by moving part of electronic density from the C-H internuclear region to the H···Rh internuclear region. This electronic redistribution is quite prominent on the RhCu(111) SAA and is also observed on pure Pt(111), but is negligible on Cu(111). For the former two materials, this electron redistribution is indicative of the pre-activation of methane upon adsorption (17).

After identifying the RhCu(111) SAA as the most promising candidate for C-H activation, we calculated the energy profile for the full dehydrogenation of methane to atomic carbon on the RhCu(111) SAA, the bare Cu(111) surface, and Pt(111), one of the most effective metals for C-H activation reactions (Fig. 1C and S3). Interestingly, the single Rh atom in the RhCu(111) SAA had an almost identical activation energy to pure Pt(111). However, unlike pure Pt(111) which stabilized CH_{2(ads)}, CH_(ads) and C_(ads) intermediates that lead to coking, the RhCu(111) SAA inherited a great deal of the coke resistance of pure Cu(111) with coke formation being exothermic on Pt(111) versus endothermic on pure Cu(111) and the RhCu(111) SAA (Fig. 1C). This is an important result given that Rh is generally not considered for dehydrogenation reactions as Rh NPs suffer from coking and hydrogenolysis is favored over selective dehydrogenation (18).

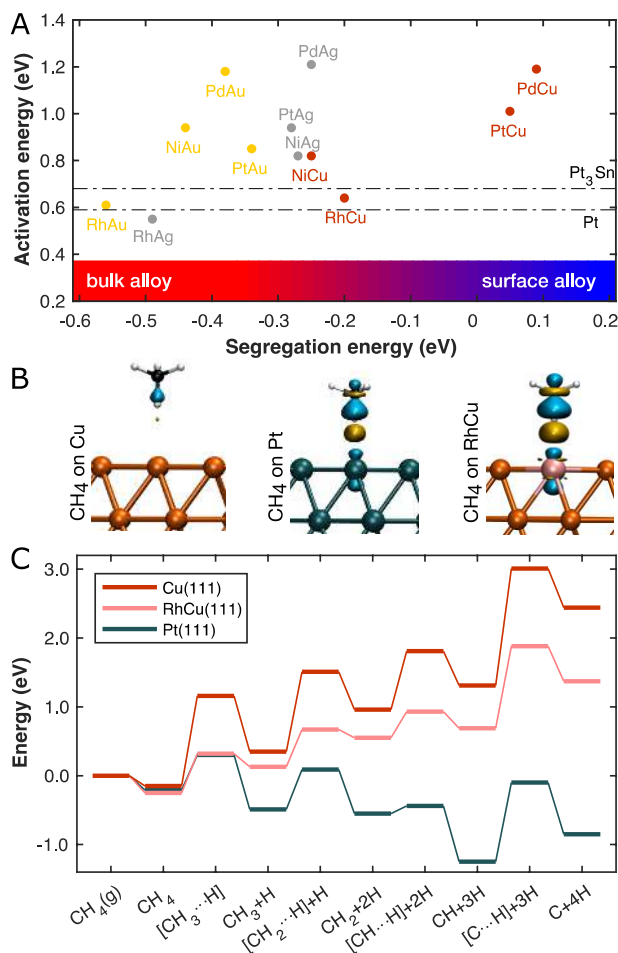
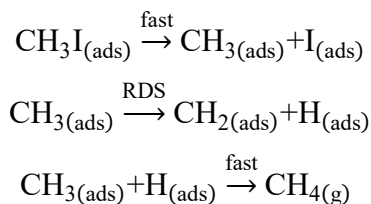


Fig. 1. Theoretical screening of SAA catalysts for C-H activation. (A) The activation energy of the first C-H cleavage in CH₄ is plotted against the segregation energy of each SAA. For comparison the activation energies on Pt(111) and Pt₃Sn(111) (2×2) are shown as dash-dotted lines. (B) Charge density difference $\Delta\rho(\mathbf{r})$ for adsorbed CH₄ on Cu(111), Pt(111) and RhCu(111) SAA. The Cu atoms are represented with orange spheres, the Pt atoms with teal, and the Rh with pink. Cyan and yellow contours represent regions of electron depletion and accumulation respectively (iso-value of ± 0.01 electron \AA^{-3}). (C) Energy profile of the sequential C-H activation steps of CH₄ on various metal surfaces (more details in Fig. S3). The energy is referenced with respect to the clean slab and CH_{4(g)}. H atoms are adsorbed on the Cu host metal in the SAA case.

To test the theoretical predictions outlined above and investigate the individual reaction steps, we performed surface science and high-resolution imaging studies of model RhCu(111) SAA catalysts. Physical vapor deposition of Rh on a Cu(111) surface held at an elevated temperature yielded atomically dispersed Rh atoms that substituted Cu atoms in the surface layer (19). A typical image of the SAA surface is given in Fig. S5. Given the low desorption barrier of methane relative to typical C-H activation barriers, we used methyl iodide (CH₃I) as a probe molecule to study C-H activation in adsorbed methyl groups on the model RhCu(111) SAA surfaces. Specifically, C-I bond cleavage is facile on Cu(111) yielding methyl groups (CH_{3(ads)}) at low temperature, which remain on the surface as it is heated. Once the rate-determining C-H activation step (RDS) occurred yielding H_(ads) and CH_{2(ads)}, gaseous methane is evolved rapidly due to facile coupling of H_(ads) and CH_{3(ads)} as seen below (20).



In this sense, methane evolution acted as a reporter of C-H activation, with lower-temperature methane evolution being associated with more facile C-H bond activation. Furthermore, the C-H activation barrier in CH₃ groups can be related to the C-H activation barrier in CH₄ via scaling relationships (see Fig. S6).

Temperature programmed desorption (TPD) experiments on Cu(111) showed that C-H activation occurred at ~430 K (Fig. 2A), consistent with previous results (20). This finding was also in good agreement with our DFT calculations which predicted that CH_{3(ads)} conversion to CH_{2(ads)} on Cu(111) had a barrier of 1.16 eV (see Fig. 1C and S3). Increasing the step density of the Cu(111) surface through argon ion sputtering resulted in a slightly lower C-H activation barrier and methane evolution at ~380 K. When individual, isolated Rh atoms were present in the Cu(111) surface as seen in the low-temperature scanning tunneling microscopy (LT-STM) image and corresponding DFT-based image simulation in Fig. 2, B and C, several new low-temperature methane evolution peaks were observed in the TPD experiments.

The lowest temperature feature at ~160 K is caused by hydrogenation of methyl groups by hydrogen from the chamber background that dissociates at Rh sites. This result was confirmed by experiments in which we pre-covered the RhCu(111) SAA surface with hydrogen before CH₃I was introduced. This low-temperature methane peak was dominant because of the aforementioned facile CH_{3(ads)} + H_(ads) → CH_{4(g)} reaction (Fig. 2A, bottom-most trace). The next TPD feature at ~300 K, was caused by C-H activation of the methyl groups to form CH_{2(ads)} and H_(ads), followed by hydrogenation of remaining methyl fragments. The temperature at which these reaction steps occurred were in good agreement with our DFT calculations, which yielded a barrier for C-H activation in CH₃ on the RhCu(111) SAA of 0.54 eV in contrast to the facile hydrogenation of CH₃ to CH₄ with has a barrier of 0.19 eV (see Fig. 1C and S3). Finally, the smaller CH₄ desorption feature at ~350 K is consistent with reaction at Cu step sites that were created during the alloying of Rh with Cu(111) (19). Full TPD traces for each experiment are given in the SM (Fig. S7).

In order to track the progression of the reaction intermediates not observable by TPD, we conducted LT-STM experiments after exposing a RhCu(111) SAA to CH₃I and annealing to different temperatures prior to 5 K STM imaging as seen in Fig. 2, D-G. After annealing to ~160 K, we observed the formation of small clusters of intact CH₃I (Fig. 2D). Heating to ~240 K resulted in the dissociation of the C-I bond resulted in CH_{3(ads)} groups and I_(ads) atoms seen in the STM images as protrusions (I_(ads)) and depressions (CH_{3(ads)}) ordered in a √3 × √3 structure, confirming the facile C-I cleavage. At ~320 K a significant fraction of the methyl groups react and desorb as CH₄ and after a ~440 K anneal, only two-dimensional islands of I atoms (bright protrusions) in a √3 × √3 structure remain (21, 22). Importantly, the image in Fig. 2G revealed that aside from I atoms, which remained adsorbed on Cu(111) until ~840 K, there was no evidence for significant coke formation, in agreement with our theoretical predictions.

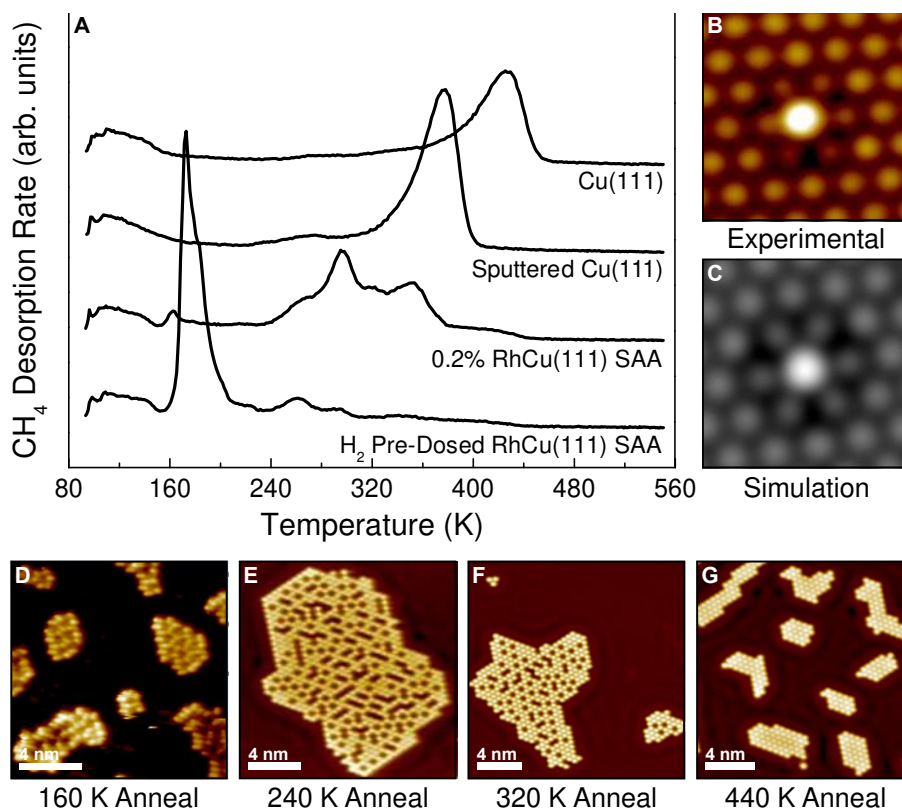


Fig. 2. Model system studies demonstrating that RhCu(111) SAAs promote low temperature C-H activation. (A) TPD experiments on Cu(111), sputtered Cu(111), 0.2% RhCu(111) SAA, and 0.2% RhCu(111) SAA pre-dosed with 200 Langmuir ($1 \text{ L} = 1 \times 10^{-6} \text{ torr} \cdot \text{s}$) of hydrogen. Each surface was exposed to 1.5 L CH₃I. (B) STM image of an isolated Rh atom in Cu(111). (C) DFT simulated STM image of an isolated Rh atom in Cu(111). (D-G) STM annealing experiments where the RhCu(111) SAA was exposed to CH₃I, annealed to the indicated temperatures, and imaged at 5 K to track the reaction progression.

Guided by our theoretical calculations and surface science studies, we synthesized RhCu/SiO₂ NP catalyst analogs with a Rh:Cu ratio of 1:100, demonstrated that they are indeed SAAs, and then tested them for the non-oxidative dehydrogenation of propane. RhCu/SiO₂ NPs of ~3 nm size were synthesized through galvanic replacement of silica-supported copper NPs (Fig. S8 and S9) by small amounts of Rh (10). CO diffuse reflectance infrared Fourier transform spectroscopy (DRIFTS) and in situ extended x-ray absorption fine structure (EXAFS) studies were performed to verify the successful alloying, as well as the absence of surface Rh aggregates. DRIFTS results (see Fig. S10 and S11) revealed a narrow (~15 cm⁻¹ full-width at half-maximum) peak corresponding to linear CO adsorption on Rh atoms at 2089 cm⁻¹. Most importantly, no IR signals for Rh directly on SiO₂ or Rh aggregates at the Cu surface were observed (23, 24), thereby demonstrating that a SAA is formed, in line with our EXAFS analysis (Fig. S12, S13, and Table S3).

We tested the RhCu/SiO₂ SAA catalyst for propane dehydrogenation in flow-reactor studies away from equilibrium in the kinetic regime. We performed a direct comparison of the RhCu/SiO₂ SAA catalyst with a standard consisting of Pt nanoparticles supported on Al₂O₃ (25). Experiments were conducted both in the absence (Fig. S14) and in the presence of hydrogen in the feed (Fig. 3A), the latter chosen to better simulate industrially relevant conditions in which a co-flow of H₂ is

required to prevent Pt from coking. The data in Fig. 3A revealed that the RhCu/SiO₂ SAA catalyst exhibited both higher activity on a per mole of active metal basis, as well as a considerably lower reaction light-off temperature compared to Pt/Al₂O₃.

The high reactivity of the RhCu/SiO₂ SAA catalyst was coupled with Cu-like propene selectivity (100% on RhCu/SiO₂ SAA versus ~80% on Pt/Al₂O₃) and resistance to coking (Fig. S15 and Table S4). While pure Rh NPs are poor dehydrogenation catalysts that are susceptible to coking because of the strong binding of carbon to extended Rh sites (18, 26), the atomic dispersion of Rh in our SAA catalysts enabled facile C-H activation while avoiding over-dehydrogenation that leads to coke formation by virtue of the endothermic nature of the coking process on single Rh atoms in a Cu host (Fig. 1C and S3). This coking resistance resulted in the active, selective and stable conversion of propane to propene and hydrogen for more than 50 hours on stream at 623 K (Fig. 3A inset).

In order to further understand these experimental observations, we used DFT to calculate and compare the reaction energetics of the RhCu(111) SAA to pure Cu(111), Rh(111), as well as Pt(111), for propane dehydrogenation. Our DFT calculations (Fig. 3B, S16, S17, and Table S5) show that the RhCu(111) SAA surface provided lower thermodynamic barriers for the formation of the iso-propyl intermediate and propene than the pure Cu(111) surface. In addition, compared to Cu(111), the SAA exhibited a considerably lower kinetic barrier for the 1st dehydrogenation step (0.57 eV on the RhCu(111) SAA versus 1.39 eV on Cu(111)) and a very small subsequent kinetic barrier for the C₃H₇ to C₃H₆ step (0.10 eV), indicative of a highly active catalyst. In fact, the activation barrier of propane on the RhCu(111) SAA is lower than on pristine Pt(111) and very similar to Rh(111) (0.68 and 0.63 eV, respectively (Fig. S16 and Table S5)). These results are in good agreement with experimental observations in which we measured the rate of propane dehydrogenation on the RhCu/SiO₂ SAA catalyst away from equilibrium over a small temperature window and found an apparent activation energy ~0.7 eV (see Fig. S18). The measured apparent activation energy was identical with and without H₂ suggesting that at these temperatures there is not a substantial coverage of H on the catalyst surface.

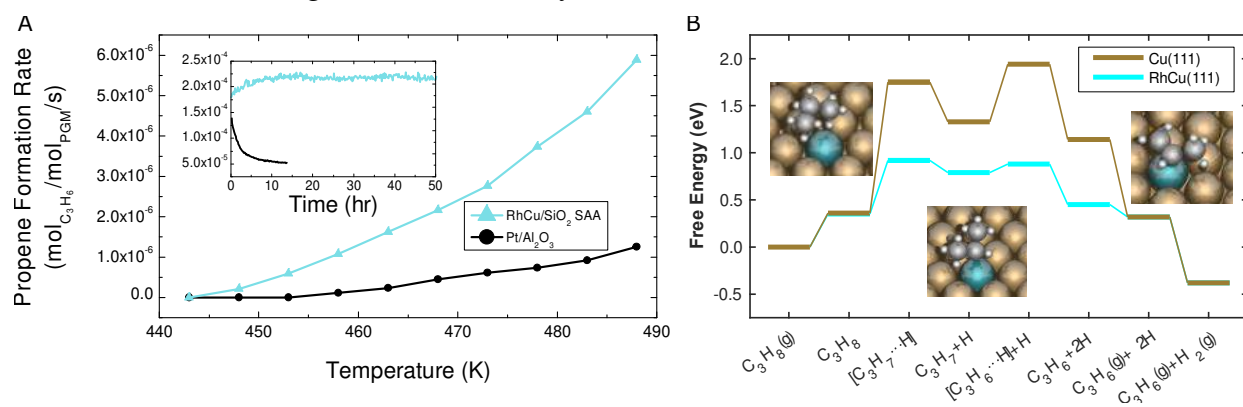


Fig. 3. Propane dehydrogenation on RhCu SAAs. (A) Propene formation rate versus temperature for the non-oxidative propane dehydrogenation reaction on RhCu/SiO₂ SAA (Rh:Cu 1:100) and Pt/Al₂O₃ catalysts. Inset: 50-hour long stability test of RhCu/SiO₂ SAA versus Pt/Al₂O₃ at 623 K. Gas composition: 1.4 kPa propane, 0.7 kPa hydrogen; 90 mL per min flow rate. (B) Free energy diagram of RhCu(111) SAA and Cu(111) for the non-oxidative dehydrogenation of propane. Free energies were calculated at 500 K for a C₃H₈ and H₂ partial pressure of 1 kPa, and 0.01 Pa for C₃H₆. The energies are referenced with respect to the clean slabs, C₃H₈(g) and H₂(g). H refers to a H atom adsorbed on the Cu metal surface.

One potential limitation in the widespread application of RhCu SAA catalysts is the well-known sintering of Cu NPs at elevated temperatures. However, despite the expected loss of reactivity because of the sintering of Cu NPs (27), measurements of the initial propane dehydrogenation rates performed at 773 K showed that the RhCu/SiO₂ SAA catalyst had a propene yield comparable to other Pt based catalysts previously reported (Table S6) (28). Furthermore, we observed that addition of 1 % Rh to the Cu NPs gave them significant sintering resistance as compared to pure Cu NPs (Fig. S8). Methods such as atomic layer deposition of thin oxide layers that are known to stabilize metal NPs against sintering at high temperatures could further address this issue (29).

References and Notes:

1. F. Besenbacher, I. Chorkendorff, B. S. Clausen, B. Hammer, A. M. Molenbroek, J. K. Nørskov, I. Stensgaard, Design of a surface alloy catalyst for steam reforming. *Science* **279**, 1913–1915 (1998).
2. S. Alayoglu, A. U. Nilekar, M. Mavrikakis, B. Eichhorn, Ru-Pt core-shell nanoparticles for preferential oxidation of carbon monoxide in hydrogen. *Nat. Mater.* **7**, 333–338 (2008).
3. M. A. Gleeson, L. B. F. Jurlink, Site-specific dissociation on Pt. *Science* **157**, 155–157 (2019).
4. F. Tao, M. E. Grass, Y. Zhang, D. R. Butcher, J. R. Renzas, Z. Liu, J. Y. Chung, B. S. Mun, M. Salmeron, G. A. Somorjai, Reaction-driven restructuring of Rh-Pd and Pt-Pd core shell nanoparticles. *Science* **322**, 932–935 (2008).
5. B. Qiao, A. Wang, X. Yang, L. F. Allard, Z. Jiang, Y. Cui, J. Liu, J. Li, T. Zhang, Single-atom catalysis of CO oxidation using Pt₁/FeO_x. *Nat. Chem.* **3**, 634–641 (2011).
6. B. C. Gates, M. Flytzani-Stephanopoulos, D. A. Dixon, A. Katz, Atomically dispersed supported metal catalysts: Perspectives and suggestions for future research. *Catal. Sci. Technol.* **7**, 4259–4275 (2017).
7. J. Hulva, M. Meier, R. Bliem, Z. Jakub, F. Kraushofer, M. Schmid, U. Diebold, C. Franchini, G. S. Parkinson, Unraveling CO adsorption on model single-atom catalysts. *Science* **379**, 375–379 (2021).
8. L. DeRita, J. Resasco, S. Dai, A. Boubnov, H. V. Thang, A. S. Hoffman, I. Ro, G. W. Graham, S. R. Bare, G. Pacchioni, X. Pan, P. Christopher, Structural evolution of atomically dispersed Pt catalysts dictates reactivity. *Nat. Mater.* **18**, 746–751 (2019).
9. G. Kyriakou, M. B. Boucher, A. D. Jewell, E. A. Lewis, T. J. Lawton, A. E. Baber, H. L. Tierney, M. Flytzani-Stephanopoulos, E. C. H. Sykes, Isolated metal atom geometries as a strategy for selective heterogeneous hydrogenations. *Science* **335**, 1209–1212 (2012).
10. R. T. Hannagan, G. Giannakakis, M. Flytzani-Stephanopoulos, E. C. H. Sykes, Single-atom alloy catalysis. *Chem. Rev.* **120**, 12044–12088 (2020).
11. M. T. Darby, M. Stamatakis, A. Michaelides, E. C. H. Sykes, Lonely atoms with special gifts: Breaking linear scaling relationships in heterogeneous catalysis with single-atom alloys. *J. Phys. Chem. Lett.* **9**, 5636–5646 (2018).
12. G. Giannakakis, M. Flytzani-Stephanopoulos, E. C. H. Sykes, Single-atom alloys as a reductionist approach to the rational design of heterogeneous catalysts. *Acc. Chem. Res.* **52**, 237–247 (2019).

13. M. T. Darby, R. Réocreux, E. C. H. Sykes, A. Michaelides, M. Stamatakis, Elucidating the stability and reactivity of surface intermediates on single-atom alloy catalysts. *ACS Catal.* **8**, 5038–5050 (2018).
- 5 14. National Academies of Science, Engineering, and Medicine, *The changing landscape of hydrocarbon feedstocks for chemical production: Implications for catalysis: Proceedings of a workshop* (The National Academy of Science, Washington, DC, 2016).
15. D. Gerceker, A. H. Motagamwala, K. R. Rivera-Dones, J. B. Miller, G. W. Huber, M. Mavrikakis, J. A. Dumesic, methane conversion to ethylene and aromatics on PtSn catalysts. *ACS Catal.* **7**, 2088–2100 (2017).
- 10 16. M. T. Darby, E. C. H. Sykes, A. Michaelides, M. Stamatakis, Carbon monoxide poisoning resistance and structural stability of single atom alloys. *Top. Catal.* **61**, 428–438 (2018).
17. V. Fung, G. Hu, B. Sumpter, Electronic band contraction induced low temperature methane activation on metal alloys. *J. Mater. Chem. A* **8**, 6057–6066 (2020).
18. J. H. Sinfelt, D. J. C. Yates, Catalytic hydrogenolysis of ethane over the noble metals of Group
15 VIII. *J. Catal.* **8**, 82–90 (1967).
19. R. T. Hannagan, D. A. Patel, L. A. Cramer, A. C. Schilling, P. T. P. Ryan, A. M. Larson, V. Çınar, Y. Wang, T. A. Balema, E. C. H. Sykes, Combining STM, RAIRS and TPD to decipher the dispersion and interactions between active sites in RhCu single-atom alloys. *ChemCatChem.* **12**, 488–493 (2019).
- 20 20. C. Chao-Ming, B. E. Bent, Methyl radical adsorption on Cu(111): Bonding, reactivity, and the effect of coadsorbed iodine. *Surf. Sci.* **279**, 79–88 (1992).
21. M. Pascal, C. L. A. Lamont, M. Kittel, J. T. Hoeft, L. Constant, M. Polcik, A. M. Bradshaw, R. L. Toomes, D. P. Woodruff, Methyl on Cu(1 1 1) - Structural determination including influence of co-adsorbed iodine. *Surf. Sci.* **512**, 173–184 (2002).
- 25 22. M. D. Marcinkowski, M. T. Darby, J. Liu, J. M. Wimble, F. R. Lucci, S. Lee, A. Michaelides, M. Flytzani-Stephanopoulos, M. Stamatakis, E. C. H. Sykes, Pt/Cu single-atom alloys as coke-resistant catalysts for efficient C-H activation. *Nat. Chem.* **10**, 325–332 (2018).
23. S. Gonzalez, C. Sousa, F. Illas, Features and catalytic properties of RhCu: A review. *Int. J. Mod. Phys. B* **24**, 5128–5138 (2010).
- 30 24. J. A. Anderson, C. H. Rochester, Z. Wang, IR study of CO adsorption on Cu-Rh/SiO₂ catalysts, coked by reaction with methane. *J. Mol. Catal. A Chem.* **139**, 285–303 (1999).
25. J. J. H. B. Sattler, J. Ruiz-Martinez, E. Santillan-Jimenez, B. M. Weckhuysen, Catalytic dehydrogenation of light alkanes on metals and metal oxides. *Chem. Rev.* **114**, 10613–10653 (2014).
- 35 26. N. Raman, S. Maisel, M. Grabau, N. Taccardi, J. Debuschewitz, M. Wolf, H. Wittkämper, T. Bauer, M. Wu, M. Haumann, C. Papp, A. Görling, E. Spiecker, J. Libuda, H. P. Steinrück, P. Wasserscheid, Highly effective propane dehydrogenation using Ga-Rh supported catalytically active liquid metal solutions. *ACS Catal.* **9**, 9499–9507 (2019).

27. M. V. Twigg, M. S. Spencer, Deactivation of copper metal catalysts for methanol decomposition, methanol steam reforming and methanol synthesis. *Top. Catal.* **22**, 191–203 (2003).
- 5 28. G. Sun, Z. J. Zhao, R. Mu, S. Zha, L. Li, S. Chen, K. Zang, J. Luo, Z. Li, S. C. Purdy, A. J. Kropf, J. T. Miller, L. Zeng, J. Gong, Breaking the scaling relationship via thermally stable Pt/Cu single atom alloys for catalytic dehydrogenation. *Nat. Commun.* **9**, 4454 (2018).
- 10 29. B. J. O'Neill, D. Jackson, A. J. Crisci, C. A. Farberow, J. Lu, P. J. Dietrich, T. Li, F. H. Ribeiro, J. T. Miller, R. Winans, J. W. Elam, J. Greeley, M. Mavrikakis, S. L. Scott, T. F. Kuech, J. A. Dumesic, Stabilization of copper catalysts for liquid phase reactions by Atomic Layer Deposition. *Angew. Chemie.* **125**, 14053–14057 (2013).
30. G. Kresse, J. Hafner, Ab initio molecular dynamics for liquid metals. *Phys. Rev. B* **47**, 558–561 (1993).
31. G. Kresse, J. Furthmüller, Efficient iterative schemes for ab initio total-energy calculations using a plane-wave basis set. *Phys. Rev. B* **54**, 11169–11186 (1996).
- 15 32. G. Kresse, J. Furthmüller, Efficiency of ab-initio total energy calculations for metals and semiconductors using a plane-wave basis set. *Comput. Mater. Sci.* **6**, 15–50 (1996).
33. M. Dion, H. Rydberg, E. Schröder, D. C. Langreth, B. I. Lundqvist, Van der Waals density functional for general geometries. *Phys. Rev. Lett.* **92**, 22–25 (2004).
- 20 34. J. Klimeš, D. R. Bowler, A. Michaelides, Chemical accuracy for the van der Waals density functional. *J. Phys. Condens. Matter.* **22**, 022201 (2010).
35. J. Klimeš, D. R. Bowler, A. Michaelides, Van der Waals density functionals applied to solids. *Phys. Rev. B* **83**, 195131 (2011).
36. J. Klimeš, A. Michaelides, Perspective: Advances and challenges in treating van der Waals dispersion forces in density functional theory. *J. Chem. Phys.* **137**, 120901 (2012).
- 25 37. P. E. Blöchl, Projector augmented-wave method. *Phys. Rev. B* **50**, 17953–17979 (1994).
38. G. Kresse, D. Joubert, From ultrasoft pseudopotentials to the projector augmented-wave method. *Phys. Rev. B* **59**, 1758–1775 (1999).
39. H. J. Monkhorst, J. D. Pack, Special points for Brillouin zone integrations. *J. Mater. Chem. A* **13**, 5188–5192 (1976).
- 30 40. D. Sheppard, R. Terrell, G. Henkelman, Optimization methods for finding minimum energy paths. *J. Chem. Phys.* **128**, 134106 (2008).
41. G. Henkelman, B. P. Uberuaga, H. Jónsson, Climbing image nudged elastic band method for finding saddle points and minimum energy paths. *J. Chem. Phys.* **113**, 9901–9904 (2000).
- 35 42. A. Heyden, A. T. Bell, F. J. Keil, Efficient methods for finding transition states in chemical reactions: Comparison of improved dimer method and partitioned rational function optimization method. *J. Chem. Phys.* **123**, 224101 (2005).
43. G. Henkelman, H. Jónsson, A dimer method for finding saddle points on high dimensional potential surfaces using only first derivatives. *J. Chem. Phys.* **111**, 7010–7022 (1999).

44. K. G. Papanikolaou, M. T. Darby, M. Stamatakis, CO-induced aggregation and segregation of highly dilute alloys: A Density Functional Theory Study. *J. Phys. Chem. C* **123**, 9128–9138 (2019).
- 5 45. X. Wei, J. Liu, G. J. Xia, J. Deng, P. Sun, J. J. Chruma, W. Wu, C. Yang, Y. G. Wang, Z. Huang, Enantioselective photoinduced cyclodimerization of a prochiral anthracene derivative adsorbed on helical metal nanostructures. *Nat. Chem.* **12**, 551–559 (2020).
46. E. Clementi, D. L. Raimondi, W. P. Reinhardt, Atomic screening constants from SCF functions. II. Atoms with 37 to 86 electrons. *J. Chem. Phys.* **47**, 1300–1307 (1967).
- 10 47. Y. Wang, K. G. Papanikolaou, R. Hannagan, D. Patel, T. Balema, L. Cramer, P. Kress, M. Stamatakis, E. C. H. Sykes, Surface facet dependence of competing alloying mechanisms. *J. Chem. Phys.* **153**, 244702 (2020).
48. D. O. Bellisario, J. W. Han, H. L. Tierney, A. E. Baber, D. S. Sholl, E. C. H. Sykes, Importance of kinetics in surface alloying: A comparison of the diffusion pathways of Pd and Ag atoms on Cu(111). *J. Phys. Chem. C* **113**, 12863–12869 (2009).
- 15 49. P. Varga, M. Schmid, Chemical discrimination on atomic level by STM. *Appl. Surf. Sci.* **141**, 287–293 (1999).
50. J. Tersoff, D. R. Hamann, Theory of the scanning tunneling microscope. *Phys. Rev. B* **31**, 805–813 (1985).
- 20 51. D. E. P. Vanpoucke, G. Brocks, Formation of Pt-induced Ge atomic nanowires on Pt/Fe(001): A density functional theory study. *Phys. Rev. B* **77**, 241308(R) (2008).
52. F. Solymosi, G. Klivényi, HREELS study of CH₃I and CH₃ adsorbed on Rh(111) surface. *J. Electron Spectros. Relat. Phenomena.* **64–65**, 499–506 (1993).
53. J. Lin, B. E. Bent, Iodomethane dissociation on Cu(111): Bonding and chemistry of adsorbed methyl groups. *J. Vac. Sci. Technol. A* **10**, 2202–2209 (1992).
- 25 54. Z. Ma, F. Zaera, Organic chemistry on solid surfaces. *Surf. Sci. Rep.* **61**, 229–281 (2006).
55. F. R. Lucci, J. Liu, M. D. Marcinkowski, M. Yang, L. F. Allard, M. Flytzani-Stephanopoulos, E. C. H. Sykes, Selective hydrogenation of 1,3-butadiene on platinum-copper alloys at the single-atom limit. *Nat. Commun.* **6**, 8550 (2015).
- 30 56. M. B. Boucher, B. Zugic, G. Cladaras, J. Kammert, M. D. Marcinkowski, T. J. Lawton, E. C. H. Sykes, M. Flytzani-Stephanopoulos, Single atom alloy surface analogs in Pd_{0.18}Cu₁₅ nanoparticles for selective hydrogenation reactions. *Phys. Chem. Chem. Phys.* **15**, 12187–12196 (2013).
57. G. Giannakakis, A. Trimpalis, J. Shan, Z. Qi, S. Cao, J. Liu, J. Ye, J. Biener, M. Flytzani-Stephanopoulos, NiAu single atom alloys for the non-oxidative dehydrogenation of ethanol to acetaldehyde and hydrogen. *Top. Catal.* **61**, 475–486 (2018).
- 35 58. J. W. Harris, J. A. Herron, J. F. DeWilde, A. Bhan, Molecular characteristics governing chlorine deposition and removal on promoted Ag catalysts during ethylene epoxidation. *J. Catal.* **377**, 378–388 (2019).

59. N. D. Subramanian, C. S. S. R. Kumar, K. Watanabe, P. Fischer, R. Tanaka, J. J. Spivey, A DRIFTS study of CO adsorption and hydrogenation on Cu-based core-shell nanoparticles. *Catal. Sci. Technol.* **2**, 621–631 (2012).
- 5 60. F. M. T. Mendes, M. Schmal, The cyclohexanol dehydrogenation on Rh-Cu/Al₂O₃ catalysts part 1. Characterization of the catalyst. *Appl. Catal. A Gen.* **151**, 393–408 (1997).
61. J. C. Matsubu, V. N. Yang, P. Christopher, Isolated metal active site concentration and stability control catalytic CO₂ reduction selectivity. *J. Am. Chem. Soc.* **137**, 3076–3084 (2015).
62. A. C. Yang, C. W. Garland, Infrared studies of carbon monoxide chemisorbed on rhodium. *J. Phys. Chem.* **61**, 1504–1512 (1957).
- 10 63. J. T. Yates, T. M. Duncan, R. W. Vaughan, Infrared spectroscopic study of activated surface processes: CO chemisorption on supported Rh. *J. Chem. Phys.* **71**, 3908–3915 (1979).
64. J. Resasco, P. Christopher, Atomically dispersed Pt-group catalysts: Reactivity, uniformity, structural evolution, and paths to increased functionality. *J. Phys. Chem. Lett.* **11**, 10114–10123 (2020).
- 15 65. B. Ravel, M. Newville, ATHENA, ARTEMIS, HEPHAESTUS: Data analysis for X-ray absorption spectroscopy using IFEFFIT. *J. Synchrotron Radiat.* **12**, 537–541 (2005).
66. J. J. Rehr, R. C. Albers, S. I. Zabinsky, High-order multiple-scattering calculations of x-ray-absorption fine structure. *Phys. Rev. Lett.* **69**, 3397–3400 (1992).
- 20 67. L. Zhou, J. M. P. Martirez, J. Finzel, C. Zhang, D. F. Swearer, S. Tian, H. Robotjazi, M. Lou, L. Dong, L. Henderson, P. Christopher, E. A. Carter, P. Nordlander, N. J. Halas, Light-driven methane dry reforming with single atomic site antenna-reactor plasmonic photocatalysts. *Nat. Energy.* **5**, 61–70 (2020).
68. A. Iglesias-Juez, A. M. Beale, K. Maaijen, T. C. Weng, P. Glatzel, B. M. Weckhuysen, A combined in situ time-resolved UV-Vis, Raman and high-energy resolution X-ray absorption spectroscopy study on the deactivation behavior of Pt and PtSn propane dehydrogenation catalysts under industrial reaction conditions. *J. Catal.* **276**, 268–279 (2010).
- 25 69. W. Zhang, H. Wang, J. Jiang, Z. Sui, Y. Zhu, D. Chen, X. Zhou, Size dependence of Pt catalysts for propane dehydrogenation: From atomically dispersed to nanoparticles. *ACS Catal.* **10**, 12932–12942 (2020).
- 30 70. J. Zhu, M. L. Yang, Y. Yu, Y. A. Zhu, Z. J. Sui, X. G. Zhou, A. Holmen, D. Chen, Size-dependent reaction mechanism and kinetics for propane dehydrogenation over Pt catalysts. *ACS Catal.* **5**, 6310–6319 (2015).
71. E. J. Jang, J. Lee, H. Y. Jeong, J. H. Kwak, Controlling the acid-base properties of alumina for stable PtSn-based propane dehydrogenation catalysts. *Appl. Catal. A Gen.* **572**, 1–8 (2019).
- 35 72. A. Hjorth Larsen, J. Jørgen Mortensen, J. Blomqvist, I. E. Castelli, R. Christensen, M. Dułak, J. Friis, M. N. Groves, B. Hammer, C. Hargus, E. D. Hermes, P. C. Jennings, P. Bjerre Jensen, J. Kermode, J. R. Kitchin, E. Leonhard Kolsbjerg, J. Kubal, K. Kaasbjerg, S. Lysgaard, J. Bergmann Maronsson, T. Maxson, T. Olsen, L. Pastewka, A. Peterson, C. Rostgaard, J. Schiøtz, O. Schütt, M. Strange, K. S. Thygesen, T. Vegge, L. Vilhelmsen, M. Walter, Z. Zeng, 40 K. W. Jacobsen, The atomic simulation environment - A Python library for working with atoms. *J. Phys. Condens. Matter.* **29**, 273002 (2017).

73. J. Shan, N. Janvelyan, H. Li, J. Liu, T. M. Egle, J. Ye, M. M. Biener, J. Biener, C. M. Friend, M. Flytzani-Stephanopoulos, Selective non-oxidative dehydrogenation of ethanol to acetaldehyde and hydrogen on highly dilute NiCu alloys. *Appl. Catal. B Environ.* **205**, 541–550 (2017).
- 5 74. J. Salmones, J. A. Wang, J. A. Galicia, G. Aguilar-Rios, H₂ reduction behaviors and catalytic performance of bimetallic tin-modified platinum catalysts for propane dehydrogenation. *J. Mol. Catal. A Chem.* **184**, 203–213 (2002).
- 10 75. G. Q. Ren, G. X. Pei, Y. J. Ren, K. P. Liu, Z. Q. Chen, J. Y. Yang, Y. Su, X. Y. Liu, W. Z. Li, T. Zhang, Effect of group IB metals on the dehydrogenation of propane to propylene over anti-sintering Pt/MgAl₂O₄. *J. Catal.* **366**, 115–126 (2018).
- 15 76. H. Zhu, D. H. Anjum, Q. Wang, E. Abou-Hamad, L. Emsley, H. Dong, P. Laveille, L. Li, A. K. Samal, J. M. Basset, Sn surface-enriched Pt-Sn bimetallic nanoparticles as a selective and stable catalyst for propane dehydrogenation. *J. Catal.* **320**, 52–62 (2014).
- 20 77. W. Cai, R. Mu, S. Zha, G. Sun, S. Chen, Z. J. Zhao, H. Li, H. Tian, Y. Tang, F. Tao, L. Zeng, J. Gong, Subsurface catalysis-mediated selectivity of dehydrogenation reaction. *Sci. Adv.* **4**, 5418 (2018).
- 25 78. O. A. Bariás, A. Holmen, E. A. Blekkan, Propane dehydrogenation over supported Pt and Pt-Sn catalysts: Catalyst preparation, characterization, and activity measurements. *J. Catal.* **158**, 1–12 (1996).
- 30 79. Y. Xu, J. Chen, X. Yuan, Y. Zhang, J. Yu, H. Liu, M. Cao, X. Fan, H. Lin, Q. Zhang, Sintering-resistant Pt on Ga₂O₃ rods for propane dehydrogenation: The morphology matters. *Ind. Eng. Chem. Res.* **57**, 13087–13093 (2018).
- 35 80. L. Rochlitz, K. Searles, J. Alfke, D. Zemlyanov, O. V. Safonova, C. Copéret, Silica-supported, narrowly distributed, subnanometric Pt-Zn particles from single sites with high propane dehydrogenation performance. *Chem. Sci.* **11**, 1549–1555 (2020).
- 40 81. P. L. De Cola, R. Gläser, J. Weitkamp, Non-oxidative propane dehydrogenation over Pt-Zn-containing zeolites. *Appl. Catal. A Gen.* **306**, 85–97 (2006).
82. Y. Zhang, Y. Zhang, Y. Zhao, T. Otroshchenko, A. Perechodjuk, V. A. Kondratenko, S. Bartling, U. Rodemerck, D. Linke, H. Jiao, G. Jiang, E. V. Kondratenko, Structure-activity-selectivity relationships in propane dehydrogenation over Rh/ZrO₂ catalysts. *ACS Catal.* **10**, 6377–6388 (2020).

Acknowledgments: R. T. H. would like to acknowledge useful conversations with Paul Kress. G. G. would like to thank Andrew Clark and Prof. Peggy Cebe for help with TGA measurements. M. S. and R. R. acknowledge Prof. Manos Mavrikakis for providing the Pt₃Sn slab for the DFT calculation. **Funding:** R. T. H., Y. W., and E. C. H. S. acknowledge funding from the Division of Chemical Science, Office of Basic Energy Science, CPIMS Program, U.S. Department of Energy, under Grant DE-SC 0004738. G.G. was supported in part by the Integrated Mesoscale Architectures for Sustainable Catalysis, an Energy Frontier Research Center funded by the U.S. Department of Energy, Office of Science, Basic Energy Sciences under award #DE-SC0012573. R.R., M.S. and A.M. acknowledge funding from the Leverhulme Trust, grant ref. RPG-2018-209. J.S. is supported by the Alexander von Humboldt Foundation, Germany through a Feodor Lynen Fellowship. J. F. acknowledges support from NSF GRFP. P. C. acknowledges support from DOE

BES DE-SC0021124. P.D. acknowledges support from National Science Foundation (Award 2034911). R.R. and J.S. thank UCL Research Computing Services and the UK Materials and Molecular Modelling Hub for computational resources, which is partially funded by EPSRC (EP/P020194/1 and EP/T022213/1). HAADF-STEM and XRF measurements made use of the MRL Shared Experimental Facilities which are supported by the MRSEC Program of the NSF under Award No. DMR 1720256; a member of the NSF-funded Materials Research Facilities Network (www.mrfn.org). **Author Contributions:** R. T. H. performed the surface science experiments and wrote the initial draft. G. G. performed the catalysts synthesis and testing. R. R. and J. S. carried out the theoretical calculations. Y. W. did the microscopy. A. M., P. D., P. C., M. F-S., M. S., and E. C. H. S. were responsible for supervision, analysis, editing and funding acquisition. **Competing interests:** Tufts University is in the process of drafting a provisional patent entitled “A Rhodium/Copper Single-Atom Alloy Heterogeneous Catalyst for the Dehydrogenation of Alkanes” on which R. T. H., G. G., and E. C. H. S. are listed as inventors. The authors declare no other competing interests. **Data and materials availability:** All data are available in the main text or the supplementary materials.

Supplementary Materials:

Materials and Methods

Supplemental Text

Figures S1-S18

Tables S1-S6

References (30-82)



Supplementary Materials for

First Principles Design of a Single-Atom Alloy Propane Dehydrogenation Catalyst

Ryan T. Hannagan, Georgios Giannakakis, Romain Réocreux, Julia Schumann, Jordan Finzel, Yicheng Wang, Angelos Michaelides, Prashant Deshlahra, Philip Christopher, Maria Flytzani-Stephanopoulos, Michail Stamatakis, E. Charles H. Sykes

Correspondence to: m.stamatakis@ucl.ac.uk and charles.sykes@tufts.edu

This PDF file includes:

Materials and Methods
Supplemental Text
Figs. S1 to S18
Tables S1 to S6

Computational Methods

The atomistic calculations were performed using periodic Density Functional Theory (DFT) as implemented in the Vienna Ab initio Simulation Package (VASP) 5.4.4 (30–32). The exchange-correlation potential was approximated with the nonlocal optB86b-vdW functional (33–36). The core electrons were modelled using the Projected Augmented Wave (PAW) approach (37, 38), and the valence density was expanded using a plane wave basis set truncated at 400 eV. We used the lattice constants determined in our previous work (13). Two slab models and Monkhorst-Pack k-point meshes were considered (39).

- A 5-layer p(3x3) slab and a 13x13x1 k-point mesh were used for the screening of single-atom alloys (SAAs) in Fig. 1A, S1, and S2 as in our previous work on SAAs (13).
- A 4-layer p(4x4) slab and 7x7x1 k-point mesh was used for all other calculations including the electronic redistribution (Fig. 1B and S4), the full activation of methane (Fig. 1C and S3) and the dehydrogenation of propane (Fig. 3B and S16).

All structures were optimized until forces were less than 0.02 eV/Å, only allowing the adsorbate and the two upmost layers of the slab to relax. Transition states were first approached using the Nudged-Elastic Band (40, 41), or the DIMER method (41–43). They were then properly optimized using the Quasi-Newton algorithm. Frequency calculations were performed for all species, freezing the coordinates of the metal atoms at their optimized values. We analyzed the frequencies of the transition states to check that they had one and only one imaginary mode. All energies were corrected for the Zero Point Energy (ZPE), except the ones shown in Fig. 1A, S1, and S2 (for consistency with our previous work).

The segregation energy ΔE_{seg} is calculated as $\Delta E_{\text{seg}} = E_{\text{bulk}} - E_{\text{SAA}}$, with E_{bulk} and E_{SAA} being the DFT-calculated energy of the surface slabs with the single atom in the bulk versus in the surface layer. For consistency with all our previous calculations of segregation and aggregation (16, 44), we use a convention by which the SAA configuration is the reference (the “starting point”), and thus, negative values signify that the atom in the bulk configuration is more stable, while positive values mean that the SAA structure is thermodynamically preferred.

The charge density difference, induced by the interaction between methane and a given metal surface, was computed based on the charge densities generated by VASP for three different structures:

- the fully relaxed structure of methane on the surface ($\text{CH}_4@M$)
- methane alone, in the exact same geometry as the adsorbed configuration ($\underline{\text{CH}_4@M}$)
- the surface alone, in the exact same geometry as the adsorbed configuration ($\underline{\text{CH}_4@M}$)

Within this approach we can add and subtract the space-dependent electronic density point-by-point using the following equation:

$$\Delta\rho(\mathbf{r}) = \rho(\mathbf{r})[\text{CH}_4@M] - \rho(\mathbf{r})[\underline{\text{CH}_4@M}] - \rho(\mathbf{r})[\underline{\text{CH}_4@M}]$$

Isosurfaces are plotted to graphically show the extent of the charge density difference using an iso-value of ± 0.01 electron \AA^{-3} . A similar value has previously been used in the literature (45).

Segregation Energy of SAAs under Reaction Conditions

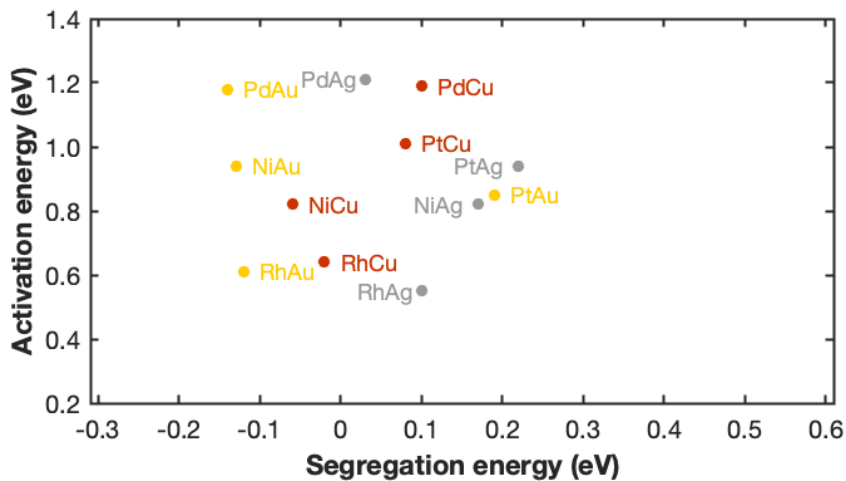


Fig. S1. Effect of adsorbed H. Activation energy of CH₄ versus segregation energy for H-covered SAA(111) surfaces.

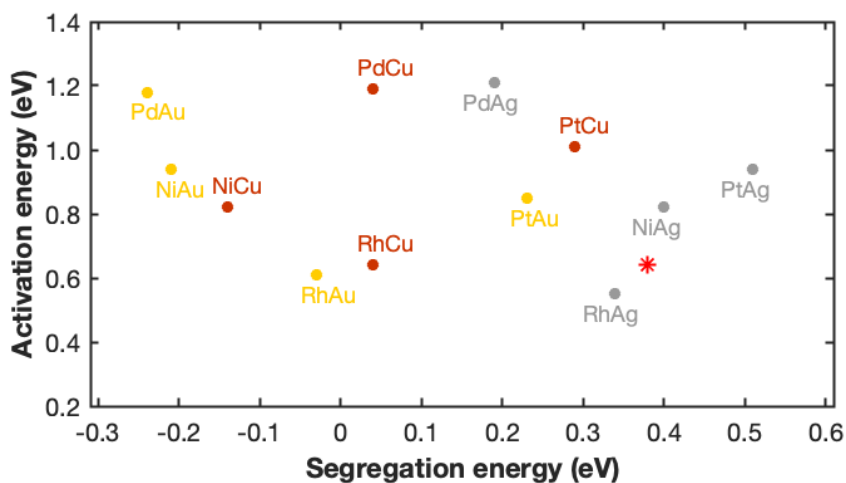


Fig. S2. Effect of adsorbed CH₃. Activation energy of CH₄ versus segregation energy for CH₃-covered SAA(111) surfaces. The red star corresponds to the segregation energy for iso-propyl covered RhCu(111) SAA.

Methane Activation on Cu(111), PtCu(111) SAA, Pt(111), RhCu(111) SAA, and Rh(111)

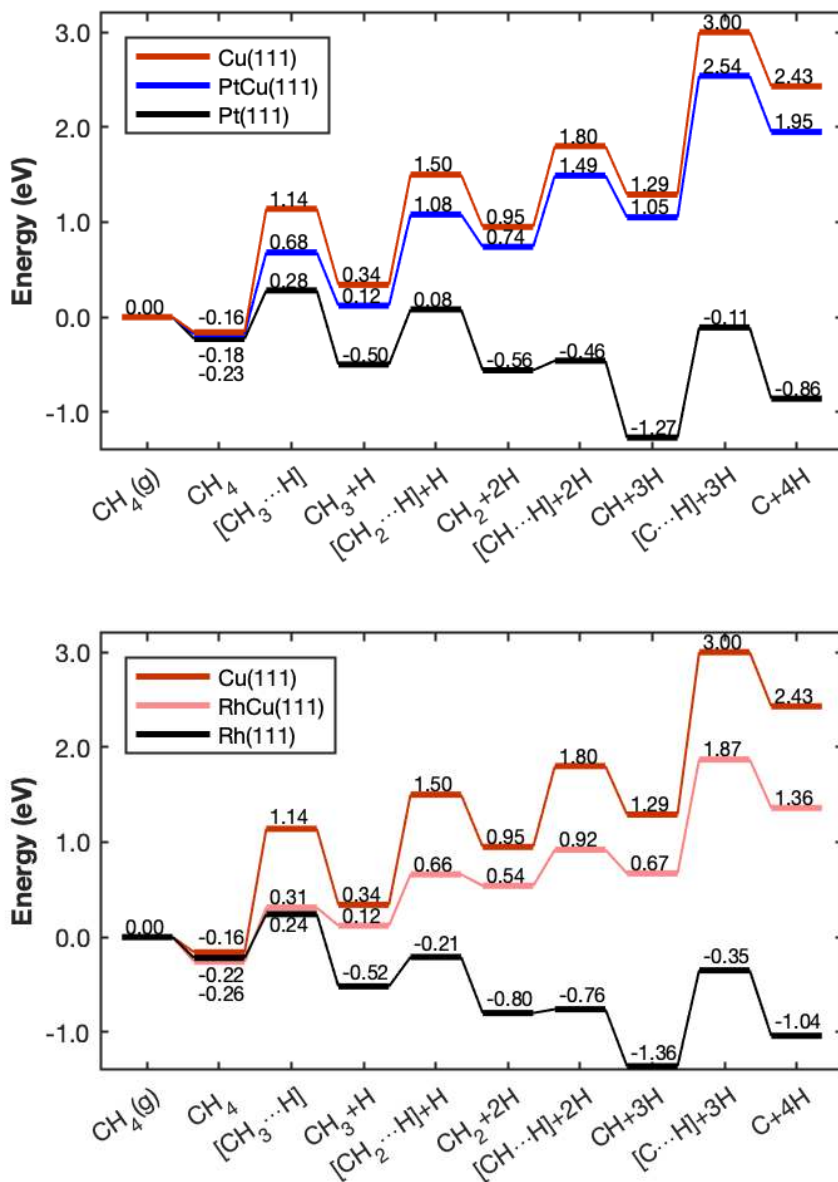


Fig. S3. Methane activation on various metal/alloy surfaces. The upper panel compares the energetics on Cu(111), PtCu(111) SAA and Pt(111). The lower panel compares the energetics on Cu(111), RhCu(111) SAA and Rh(111). All reported energies are ZPE corrected.

Alternate Representation of Charge Difference Density

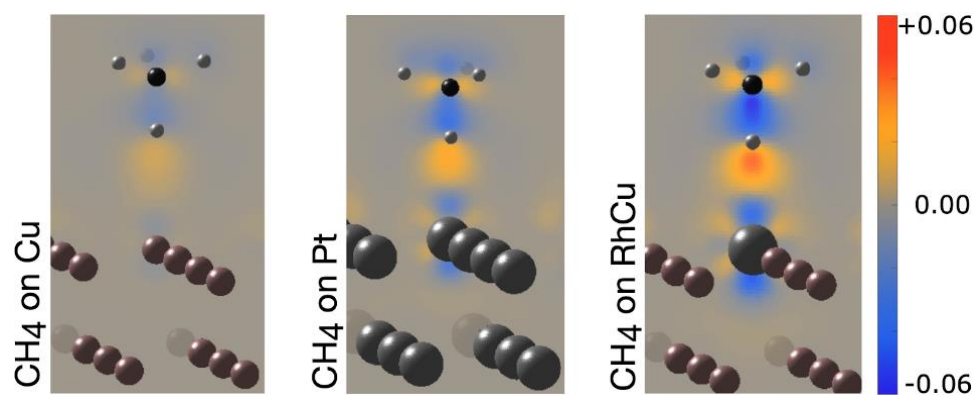


Fig. S4. Plot of two-dimensional slice through the charge density difference $\Delta\rho(\mathbf{r})$: (in electron \AA^{-3}) for adsorbed methane on Cu(111), Pt(111) and RhCu(111) SAA.

Methane Adsorption Geometries

Table S1. Adsorption geometries and energies of CH₄ on Pt(111), Rh(111) and RhCu(111) SAA. The energies are corrected for ZPE.

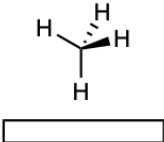
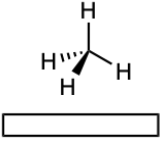
Geometry	Pt (eV)	Rh (eV)	RhCu (eV)
	-0.225	-0.217	-0.264
	-0.215	-0.206	Not a minimum on the potential energy surface

Table S2. Geometric parameters of methane in the most stable adsorption configuration on various metal/alloy surfaces. $r_A(X)$ is the atomic radius of atom X (46).

Distances (Å)	Cu(111)	Pt(111)	PtCu(111)	Rh(111)	RhCu(111)
C–H	1.104	1.114	1.110	1.113	1.120
H...M	2.466	2.286	2.431	2.235	2.113
$r_A(H) + r_A(M)$	1.98	2.30		2.26	

Surface Science Methods

Temperature programmed desorption (TPD) experiments were conducted in a custom-built ultra-high vacuum (UHV) chamber pumped by a combination of a Pfeiffer Vacuum turbo molecular pump (Model TC 400) and titanium sublimation pumps resulting in a base pressure of less than 1×10^{-10} mbar. The chamber is equipped with a Hidden Hal RC 201 mass spectrometer capable of being advanced to less than 1 mm from the sample face. All the surface science experiments were performed on a Cu(111) single crystal (Princeton Scientific) which was cleaned by repeated cycles of argon ion sputtering (5×10^{-5} mbar argon, 1.5 keV beam energy, $\sim 2 \mu\text{A}$ drain current, RBD sputter gun) and thermal annealing to 720 K. The crystal was heated resistively and cooled with liquid nitrogen. Temperatures were measured using a K-type thermocouple welded to the back of the crystal. All TPD experiments were conducted with a linear heating rate of 2 K/s. Deposition of CH_3I (purchased from Sigma-Aldrich 99% purity and further purified by repeated freeze pump thaw cycles) was performed using a precision leak valve onto the sample held at 90 K. Exposures of hydrogen were done via a collimated molecular doser attached to the leak valve with the sample held at 200 K. Alloys were prepared by deposition of Rh (Goodfellow, 99.9% purity) onto Cu(111) held at elevated temperature (420 K) using an electron beam evaporator (Omicron, EFM 3) (19). Rh coverages in TPD experiments were calculated based on comparison of CO desorption from the Rh sites versus saturated CO on Cu(111).

Scanning tunneling microscopy (STM) experiments were conducted using an Omicron low-temperature STM comprised of a preparation chamber (base pressure of less than 2×10^{-10} mbar) and a STM chamber (base pressure of less than 1×10^{-11} mbar). Both chambers are pumped with a series of turbomolecular pumps, ion pumps, and titanium sublimation pumps. Experiments were conducted on a Cu(111) crystal (Princeton Scientific) which was cleaned by repeated cycles of argon ion sputtering (5×10^{-5} mbar argon, 1.5 keV beam energy, $\sim 1 \mu\text{A}$ drain current, RBD sputter gun) and thermal annealing to 1000 K. All molecular deposition was performed with a collimator attached to a leak valve onto the sample held at 5 K before annealing to the indicated temperatures and cooling back to 5 K for STM imaging. The CH_3I source was the same as described above. Etched tungsten STM tips were used and typical imaging conditions for CH_3I were ~ 100 mV and ~ 100 pA. Alloys were prepared by deposition of Rh onto the Cu(111) crystal held at an elevated temperature (~ 420 K) via electron beam evaporation as discussed above. Rh coverages for the STM experiments were calculated by counting the number of Rh atoms and comparing to the total number of surface atoms. Image processing was done using SPIP.

Typical Image of the Model RhCu(111) SAA Surface

Fig. S5 shows a typical STM image taken after deposition of $\sim 0.5\%$ monolayer (ML) Rh into the surface of Cu(111) at ~ 420 K and cooling to image. Here, the isolated Rh sites appear in STM images as depressions found mostly in “brims” above step edges (19). This is due to the alloying mechanism which favors diffusion of the Rh to step edges followed by place exchange into the terrace above the step edge in brims, rather than direct place exchange (19, 47, 48). The Rh atom sites appear in STM images as either protrusions or depression depending on imaging conditions and the STM tip state (49).

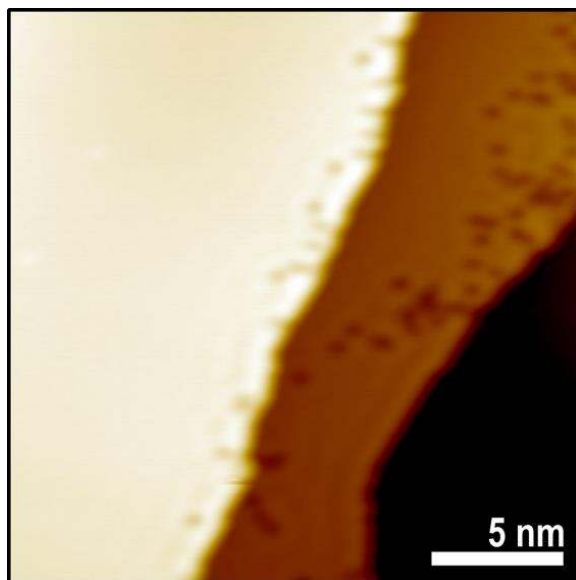


Fig. S5. 80 K STM image of $\sim 0.5\%$ ML RhCu(111) SAA surface. Image conditions: 300 mV and 300 pA.

Linear Scaling Relationship between C-H Activation in CH₄ and CH₃

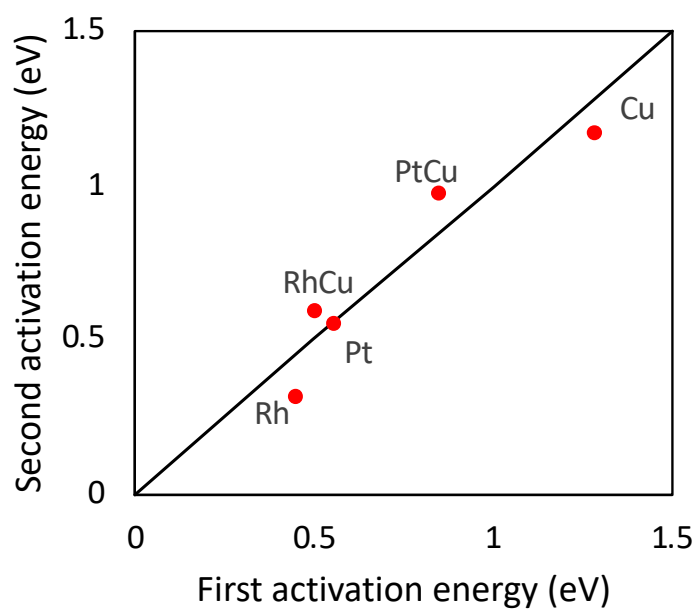


Fig. S6. Correlation between DFT calculated first ($\text{CH}_4 \rightarrow \text{CH}_3 + \text{H}$) and second ($\text{CH}_3 \rightarrow \text{CH}_2 + \text{H}$) C-H activation barriers.

STM Simulation

The DFT simulated STM image in Fig. 2C was produced from a larger 4-layer p(5x5) slab. According to the Tersoff-Hamann method, the tunneling-current in an STM experiment is equivalent to the local density of states (50). From the pre-converged clean RhCu(111) SAA slab, the partial charge density was evaluated in an energy range of 0.0 - 1.0 eV relative to the Fermi energy. The partial charge density file from VASP was read by the HIVE-STM program (51), and an image of the surface of constant charge density at a value of $5 \times 10^{-3} \text{ e}\text{\AA}^{-3}$ was obtained and is shown in Fig. 2C.

Expanded TPD Results

Fig. S7 shows full TPD traces from the experiments shown in Fig. 2A. During these experiments, masses characteristic of all products which have been observed to desorb from Cu(111) and Rh(111) in the literature were tracked. These are as follows: hydrogen (m/z 2), methyl groups (m/z 15), methane (m/z 16), ethene (m/z 27), ethane (m/z 30), propene (m/z 41), and methyl iodide (m/z 142) (52–54). At the surface coverages studied, the primary products observed from both Cu(111) and the RhCu(111) SAA were methane, ethene and propene. We did not observe the high temperature methyl rejection pathway based on the comparison of m/z 16 and m/z 15 which in our case were consistent with the production of pure methane (20).

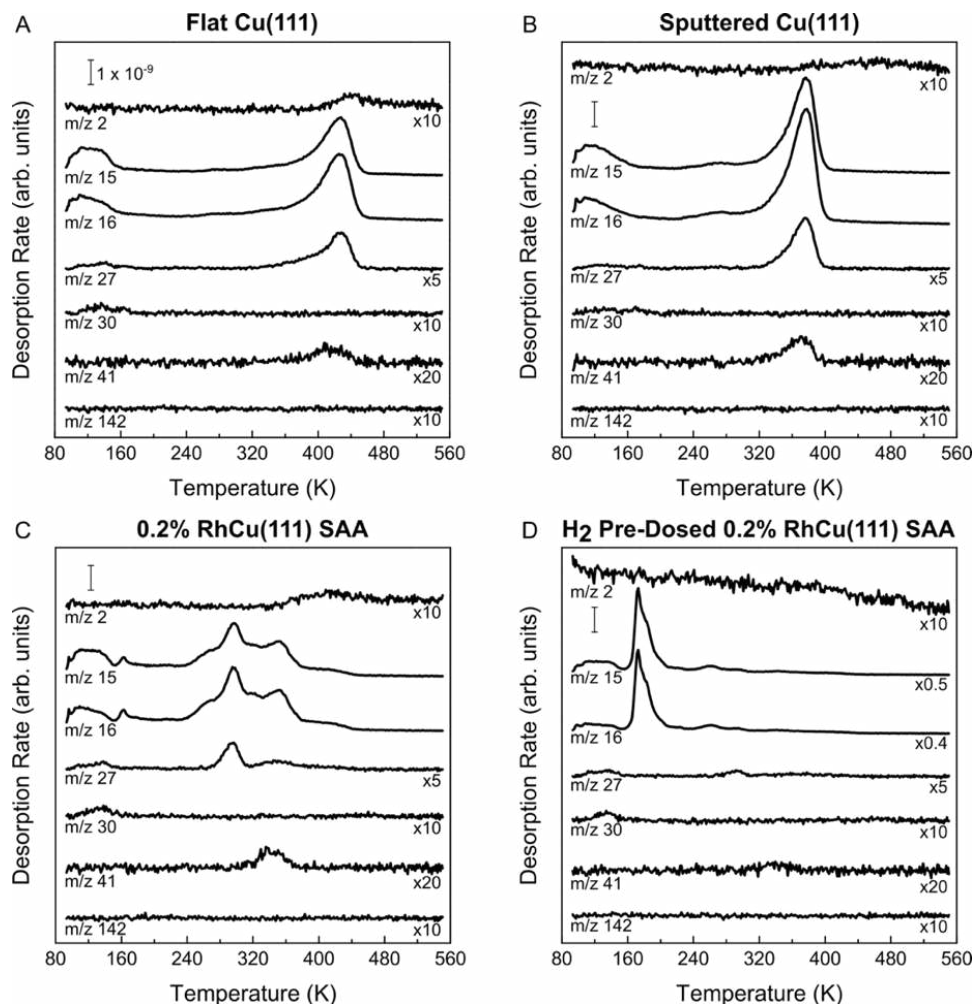


Fig. S7. TPD traces for hydrogen (m/z 2), methyl groups (m/z 15), methane (m/z 16), ethene (m/z 27), ethane (m/z 30), propene (m/z 41), and methyl iodide (m/z 142) from model surfaces.

On Cu(111), we observed the desorption of methane, ethane, and propene rate-limited by conversion of CH_3 to CH_2 . Once this first C-H activation step occurs, the remaining reaction steps to form methane, ethene, and propene are facile. A similar result is seen on a sputtered Cu(111) surface which contains more undercoordinated Cu step and kink sites and the C-H activation occurs at a slightly lower temperature than on flat Cu(111). Addition of small amounts of Rh atoms to Cu(111) shifts the C-H activation significantly lower in temperature than on pure Cu as evidenced by the low temperature evolution of methane at ~ 300 K. To confirm that the

hydrogenation of methyl groups to methane occurs at very low temperature, we pre-covered the surface with hydrogen. We observed low temperature methane evolution (~170 K) limited only by the amount of hydrogen available on the surface, confirming that methyl hydrogenation is more facile than methyl C-H activation.

Nanoparticle Catalyst Synthesis

RhCu/SiO₂ SAA catalysts were prepared via the galvanic replacement reaction, which has been previously described as a promising method for the synthesis of Cu-based SAAs (10, 55, 56). Copper nanoparticles (NPs) were prepared in colloidal form by reducing Cu(NO₃)₂ in aqueous solution with ascorbic acid and NaBH₄ as the reducing agents and polyvinylpyrrolidone as the capping agent. The resulting Cu NPs were deposited onto a silica support (fumed silica, 0.2–0.3 μm average aggregate particle size, surface area 200 m²/g, calcined in air at 873 K prior to use) followed by vacuum filtration, drying in vacuo, and calcination in air at 573 K. Cu/SiO₂ with 2.5% metal loading was formed, as confirmed by inductively coupled plasma (ICP) measurements. Addition of appropriate amounts of RhCl₃ on pre-reduced Cu/SiO₂ suspended in aqueous solution facilitated the selective deposition of Rh atoms in the Cu NP surfaces via the galvanic replacement reaction. The acidic pH of RhCl₃ solutions and acidic point of zero charge on SiO₂ mitigated the potential electrostatic deposition of Rh directly onto SiO₂. This is evidenced by the CO IR measurements below. The galvanic replacement reaction proceeds via exchange of the metal host atoms with the minority Rh metal precursor. The lower reduction potential of the host metal, Cu, (Cu²⁺/Cu⁰, E⁰ = 0.337 V) relative to that of the metal precursor, Rh, (Rh³⁺/Rh⁰, E⁰ = 0.8 V) results in the thermodynamically favorable reduction of the Rh precursor by the Cu metal surface (2Rh³⁺ + 3Cu⁰ → 2Rh⁰ + 3Cu²⁺, E⁰ = 0.49 V). The atomic ratio of Rh to Cu was 1:100 in the RhCu/SiO₂ SAA catalysts, as verified via ICP measurements.

Catalyst Testing under Non-Oxidative Propane Dehydrogenation Conditions

Catalytic activity tests were performed at atmospheric pressure in a U-shaped quartz tube (1/4" outside diameter) with a bulb and a quartz frit upon which the catalyst samples were placed. The reactor was heated using a resistive furnace with ceramic insulation (National Element, FA120) and the temperature was measured using a thermocouple (Omega, K-type) connected to a temperature controller (Watlow, EZ-Zone). Flow rates of He (99.999%, Airgas), propane (99.99%), and H₂ (supplied via an H2PEM-165 hydrogen generator) were set using electronic mass-flow controllers (Porter 601 CV Series II). Reactant and product concentrations were measured by gas chromatography (Agilent 7890B). Propane, propene, ethane, ethylene, methane and all other possible hydrocarbon byproducts were separated using an HP-PLOT Q capillary column (30 mm × 0.32 mm × 20.00 μm) and quantified using a flame ionization detector. H₂, CO, and CO₂ were separated on a Carboxen-1000 packed column and quantified using a thermal conductivity detector. It should be noted that particular attention was paid to ensure operation away from equilibrium (<5% equilibrium conversion) for the kinetic measurements, while stability tests were performed at ~30-40% equilibrium conversion. Carbon balance was ~97% for all measurements. Prior to testing, all catalysts were reduced under a 20 mL·min⁻¹ flow of H₂ (10% balanced in He) at 673 K for 2 hr.

High-Angle Annular Dark-Field Scanning Transmission Electron Microscopy

The size of the catalyst NPs was measured via high-angle annular dark-field scanning transmission electron microscopy (HAADF-STEM) using a ThermoFisher Talos G2 200X microscope with an accelerating voltage of 200 kV. RhCu/SiO₂ samples reduced at 623 K under H₂ showed small particles on the order of ~3 nm (Fig. S8A). Resolving Rh atoms in Cu is not feasible at present via scanning transmission electron microscopy due to similar mass of the two elements ($Z=29$ for Cu and 45 for Rh). To demonstrate the improved sintering resistance of the Cu metal host after 1% Rh atom doping, we performed HAADF-STEM imaging and compared the data to a pure Cu/SiO₂ catalyst treated under the same conditions. The remarkable improvement in the sintering resistance of the host Cu particle by the addition of the dopant Rh metal atom can be seen by comparing images of Cu/SiO₂ reduced in H₂ at 623 K (Fig. S8C) to the RhCu/SiO₂ sample also reduced at in H₂ 623 K (Fig. S8A). The Cu/SiO₂ images clearly show the growth of larger Cu particles, a considerable deviation from the smaller particle size of the RhCu/SiO₂ SAAs after the same treatment. The difference is even greater when comparing the samples tested at 723 K under reaction conditions (Fig. S8B and D). A few clusters of increased particle size are evident for the RhCu/SiO₂ SAA sample in Fig. S8B, accounting for the drop in reactivity at elevated temperatures (above ~673 K), described in the main text. In contrast, imaging of the pure Cu/SiO₂ sample revealed significant host particle growth with some aggregates several orders of magnitude in size (~1 μm) larger than particles in the RhCu/SiO₂ sample (Fig. S8D). The beneficial effect of Rh atom doping in suppressing the sintering of the host metal is in line with previous studies of NiAu SAAs (57).

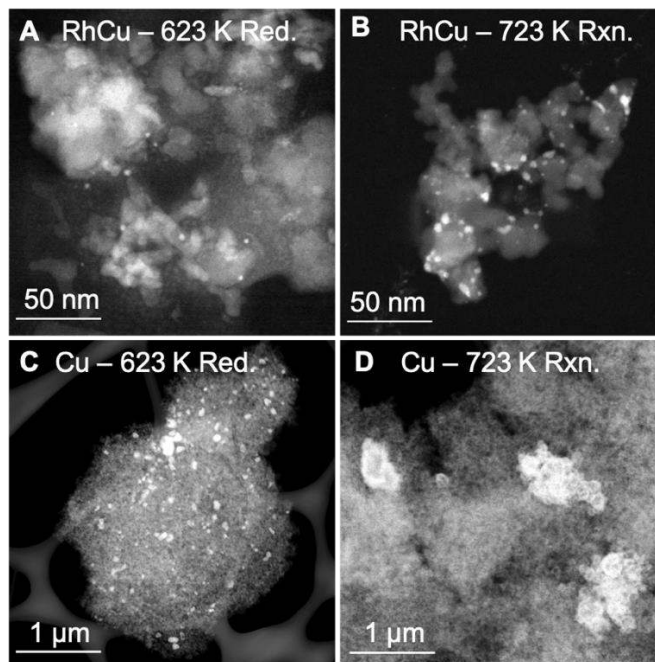


Fig. S8. HAADF-STEM images of the RhCu/SiO₂ catalyst after H₂ reduction (Red.) and reaction (Rxn.) conditions. RhCu/SiO₂ catalyst (A) after reduction at 623 K and (B) after exposure to propene dehydrogenation reaction conditions at 723 K. Cu/SiO₂ catalyst (C) after reduction at 623 K and (D) after reaction at 723 K. Due to the heavier mass of Cu (or RhCu) as compared to Si or O, Cu/RhCu particles appear as brighter areas on the SiO₂ support. Note that the scale bars for A and B are 50 nm and the scale bars for C and D are 1 μm . This 20x difference demonstrates a significant sintering of the pure Cu catalyst that is drastically reduced by the presence of 1% Rh.

Chloride Residues on Catalysts

To determine if catalyst samples contained a significant amount of remnant chlorine that could influence reactivity, wavelength dispersive x-ray fluorescence (WDXRF) was performed using a Rigaku ZSX Primus IV spectrometer. Powder catalysts were pressed into self-supporting pellets and spectra of the $K\alpha$ fluorescence lines were recorded for Si, O, Cu, and Cl. A PET crystal (8.742 Å) was used for Si and Cl while a graphite crystal (6.708 Å) and LiF 200 crystal (4.027 Å) were used for O and Cu, respectively. Rh was not scanned due to interference with the Rh X-ray source.

The XRF analysis showed ~200 ppm of Cl in the freshly reduced RhCu/SiO₂ SAA catalyst (Fig. S9) and that Cl species have two orders of magnitude lower abundance than in Cu. Given the ~3 nm diameter metal particles with ~33% dispersion, if all the Cl in the sample were at the surface of metal nanoparticles this would result in ~3% of a monolayer of Cl. This amount of Cl is unlikely to have a significant impact on the catalysis as previous studies have shown that Cl has a minimal effect as a promoter until concentrations approach a significant fraction of a monolayer (58). Furthermore, Cl typically acts to either block active sites and/or promote sintering, which in the context of the current reaction chemistry, would act to decrease activity and stability. Therefore, we do not expect that Cl plays a significant role on the observed catalytic behavior.

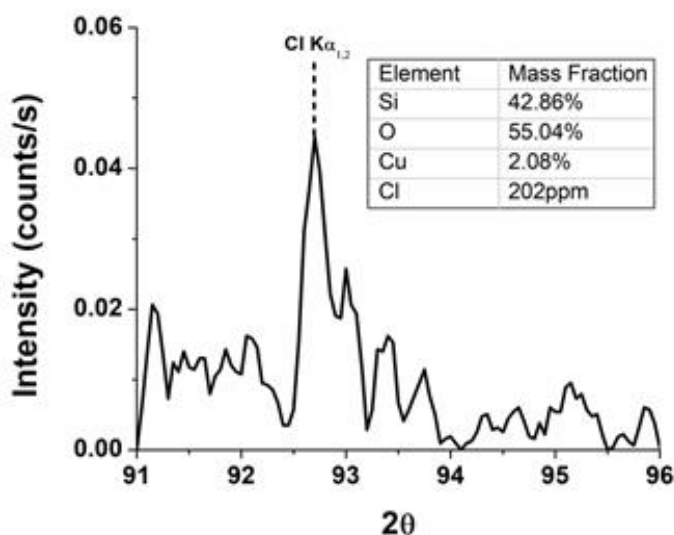


Fig. S9. WDXRF analysis of RhCu/SiO₂ catalyst. XRF spectra of the region corresponding to the Cl $K\alpha$ fluorescence (92.76° with a PET crystal, 8.742 Å) and the semi-quantitative sample composition (inset).

CO Diffuse Reflectance Infrared Fourier Transform Spectroscopy

Diffuse reflectance infrared Fourier transform spectroscopy (DRIFTS) measurements, using CO as a probe molecule, were conducted on a Thermo Scientific Nicolet iS50 DRIFTS spectrometer with a Praying Mantis high temperature reaction chamber. The samples were first reduced in the DRIFTS cell under 20% H₂ in Ar at 673 K for 1 hour. The cell was then purged with He and CO was introduced into the cell at room temperature. Background spectra were collected before and after reduction, as well as after CO chemisorption. Fig. S10A shows the DRIFTS spectra for the RhCu/SiO₂ SAA with CO chemisorption at room temperature. The peak at 2122 cm⁻¹ is assigned to linearly adsorbed CO on the Cu NPs. This assignment was verified by similar experiments on Cu/SiO₂ (Fig. S10B). The higher wavenumber peak (2134 cm⁻¹) is ascribed to Cu⁺-CO interactions (59). Similar IR features have previously been reported on other RhCu alloys (24, 60). By examining the region below 2100 cm⁻¹, we can draw conclusions about the Rh structures present on the catalyst surface. For comparison, the DRIFTS spectra for pure Rh NPs and atomically dispersed Rh species in a Rh/SiO₂ sample (Fig. S10C) show peaks at 2033 and 2094 cm⁻¹, corresponding to the symmetric and antisymmetric stretching of CO in Rh gem-dicarbonyl (Rh(CO)₂) species (61, 62). The feature at 2063 cm⁻¹ that shifts with coverage is attributed to atop adsorption of CO on Rh atoms in Rh aggregates. Furthermore, a broad peak at 1895 cm⁻¹, characteristic of bridge bound CO on contiguous Rh surfaces is observed for the Rh/SiO₂ samples (63). In contrast to Rh NPs, none of these features are observed for RhCu/SiO₂ SAA catalysts. This result provides verification that Rh aggregates are not present on the surface of the RhCu/SiO₂ SAA samples, as well as a lack of Rh atoms deposited on the support during the synthesis process, confirming the suitability of the galvanic replacement reaction for the selective decoration of Cu NPs with Rh atoms. The lack of Rh-related peaks from Fig. S10A indicates that Rh atoms are not present in the surface of Cu when the IR experiment is performed at room temperature, in agreement with the Extended X-ray absorption fine structure (EXAFS) results (see below). However, surface segregation of Rh atoms can be induced by CO. Fig. S10D shows the DRIFTS spectra of RhCu/SiO₂ treated at 373 K under CO. Comparing these spectra to Fig. S10A, a sharp feature at 2089 cm⁻¹ is seen, consistent with CO binding atop to isolated Rh atoms (61). The full width at half maximum (FWHM) value for this peak (Fig. S10D inset) is ~15 cm⁻¹, indicative of site homogeneity, and consistent with Rh atoms that are isolated from one another in the copper surface (64). Furthermore, this CO peak does not shift as the CO coverage is changed, which indicates small dipole-dipole interactions, as would be expected for highly dispersed Rh atoms in Cu.

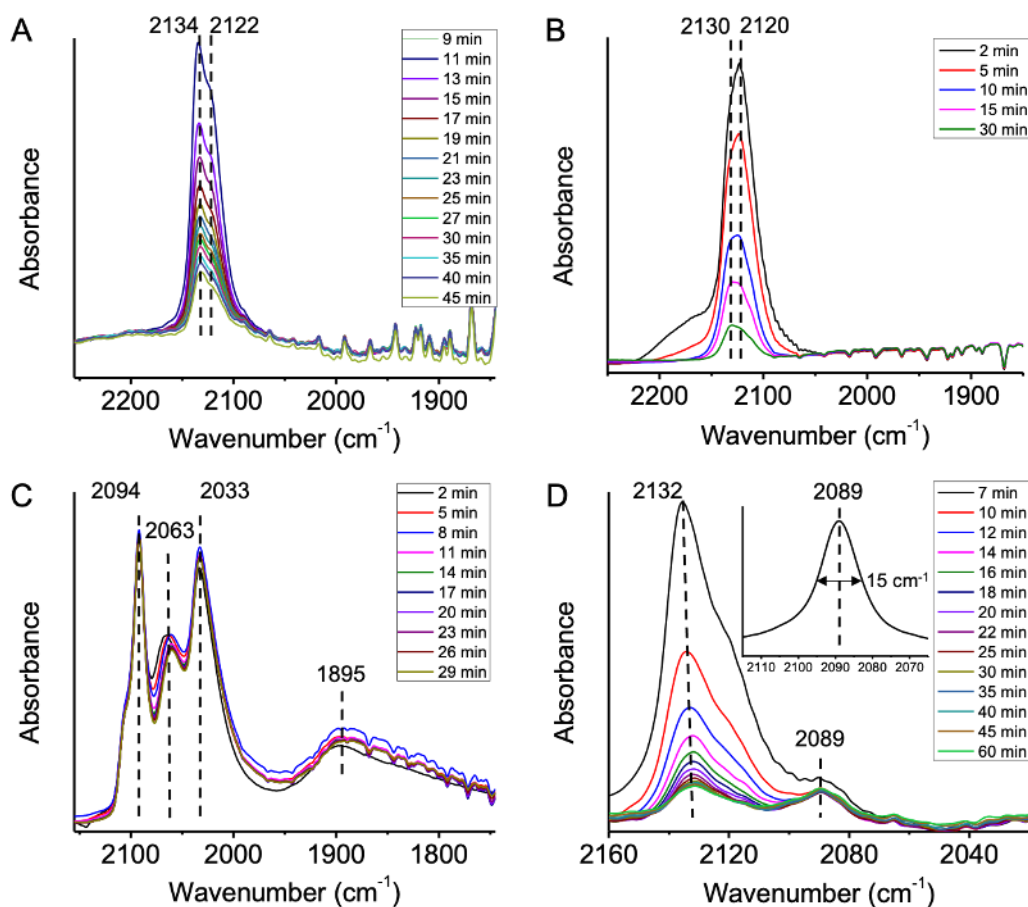


Fig. S10. DRIFTS spectra of room temperature adsorbed CO on (A) RhCu/SiO₂ SAA, (B) Cu/SiO₂, and (C) Rh/SiO₂. (D) RhCu/SiO₂ SAA exposed to CO at 373 K. All spectra were collected at room temperature. The time values on the graphs represent the length of the He gas purge after CO exposure.

To probe the composition of the surface layer of the catalyst after the propane dehydrogenation reaction we performed room temperature CO-IR measurements after exposure to reaction conditions. Specifically, after reaction the RhCu/SiO₂ sample was cooled to room temperature in helium before exposure to CO in order to decouple the well-known tendency of CO to induce surface segregation in alloys. The data shows the presence of an IR peak at 2089 cm⁻¹ consistent with CO adsorption atop Rh atoms in the surface of Cu that was not present in the as synthesized samples, demonstrating that the Rh atoms are stabilized at the surface under reaction conditions due to the effect of iso-propyl intermediates reversing the tendency of Rh to exist in the bulk (see Figs. 1, S1, S2, and S11).

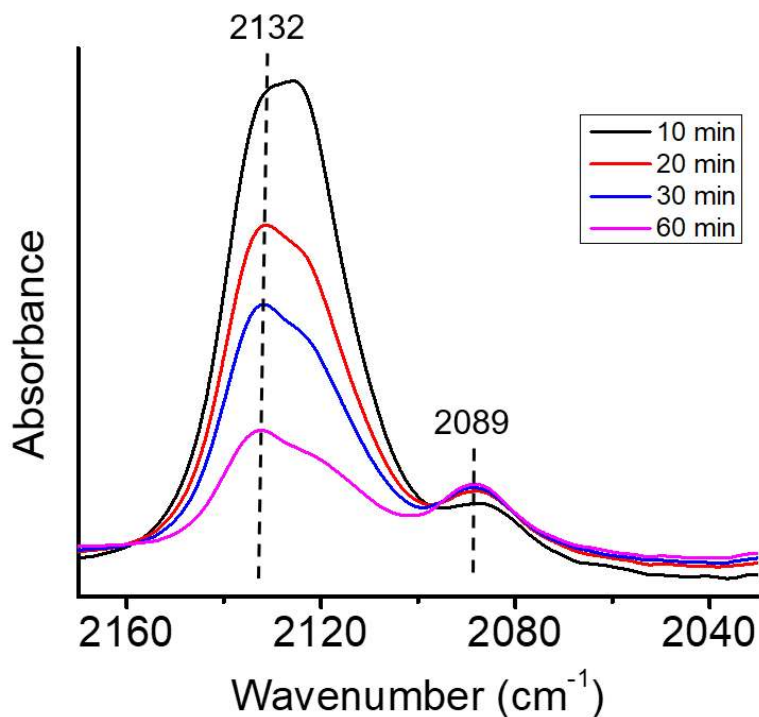


Fig. S11. DRIFTS spectra of CO on the RhCu/SiO₂ SAA after in situ exposure to reaction mixture (5 kPa propane, 5 kPa H₂, balance in He) at 623 K. The reduced sample was exposed to reaction conditions at 623 K for 1 hr in the DRIFTS cell, followed by cooling to room temperature under reactants. Subsequently, the cell was purged with He for 30 min, followed by CO adsorption at room temperature. Spectra were obtained at room temperature during CO desorption (cell purged with He). The time values on the graph represent the length of the He gas purge after CO exposure.

Extended X-Ray Absorption Fine Structure

X-ray absorption spectroscopy (XAS) measurements of the Rh K-edge (23,220 eV) were conducted at beamline 12-BM at the Applied Photon Source, Argonne National Laboratory. The RhCu/SiO₂ SAA catalyst sample was reduced in situ at 673 K under H₂ for 1 hour, cooled to room temperature and purged with He. Spectra were collected in fluorescence mode under He flow at room temperature. Rh foil was scanned simultaneously for energy calibration.

The raw data were processed using the Athena interface of the Demeter software package, (65) where spectra were energy calibrated, merged, and normalized. EXAFS fitting was performed taking into account k^1 -, k^2 -, and k^3 - weighting using the Artemis interface of Demeter. Phase shifts and amplitude for relevant backscattering paths were calculated using FEFF6 (66). S_0^2 was determined to be 0.74 +/- 0.04 by fitting a Rh foil standard (Fig. S12). A RhCu alloy model was used to generate Rh-Cu and Rh-Rh scattering paths by modifying a face-centered cubic (FCC) Cu crystal structure (mp-30).

The model that gave the best fit to the RhCu catalyst data after a 673 K H₂ reduction consisted of 2 scattering paths: Rh-Cu (coordination number 9.0 +/- 1.1) and Rh-Rh (coordination number 3.1 +/- 0.9) for a total coordination number of 12.1 +/- 1.4 (Fig. S13 and Table S3). Typically for such small particles (see Fig. S8) we would expect a lower total coordination number. However, this data is consistent with bulk Rh in a FCC lattice after high temperature H₂ reduction. This suggests that pretreatment in H₂ does not stabilize Rh atoms in the surface of the Cu NPs (in agreement with our earlier theoretical results and the infrared spectroscopy experiments above). In the bulk, Rh atoms aggregate, resulting in some Rh-Rh coordination as observed from this sample averaged EXAFS measurement. The EXAFS analysis is consistent with the IR spectra in Fig. S10A, as well as the calculations in Fig. S1, where CO adsorption on Rh was not observed following reduction in H₂, indicating that Rh resides in the bulk of the Cu particles after high temperature H₂ reduction.

Previous calculations indicate that it is energetically unfavorable for Rh atoms at the surface of a RhCu dilute alloy to aggregate (16). Additionally, the presence of carbonaceous adsorbates, such as those present under reaction conditions, further stabilize dispersed dopant species at the particle surface as was shown previously for RuCu SAAs (67). Taken together, the DRIFTS data and XAS analysis provide strong evidence that Rh exists as isolated atoms in the Cu NP surface when exposed to carbonaceous species at elevated temperature.

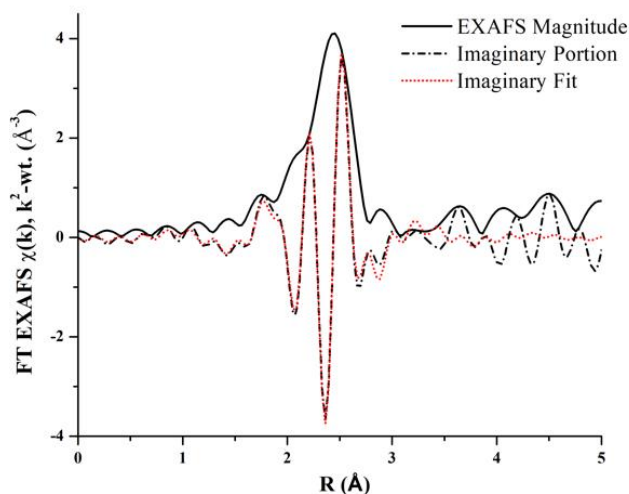


Fig. S12. Fitting for the Rh L3 edge of Rh metal foil used to determine S_0^2 for EXAFS fitting of RhCu/SiO₂ samples. Fits were performed over a k range of 3-14 Å⁻¹ and an R range of 1.0-2.75 Å.

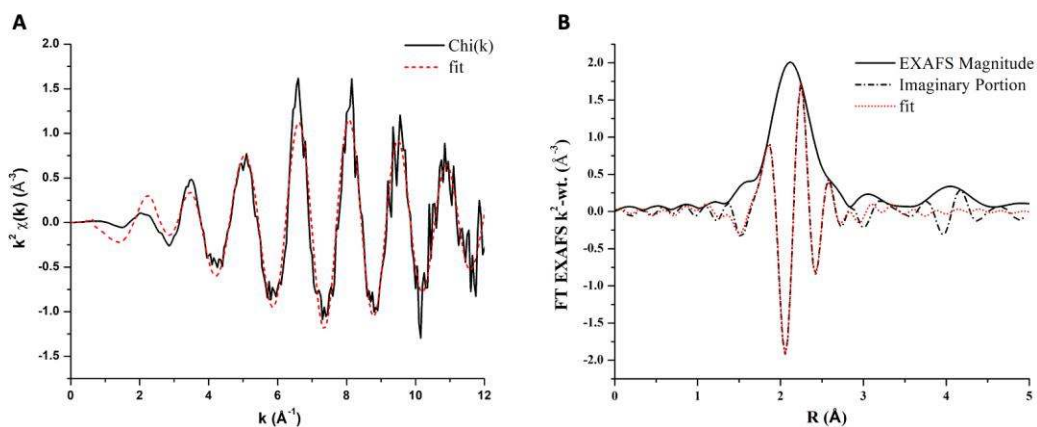


Fig. S13. (A) EXAFS spectra in k -space of RhCu/SiO₂ after in-situ reduction at 673 K under H₂ for 1 hour. The fit is shown as a red dotted line and was performed using a Hanning window over a k range 3-12 Å⁻¹. (B) The Fourier transform (FT) EXAFS spectra of the spectra in panel (A) with fits performed over an R range 1.3-2.8 Å. Black dashed line shows the imaginary portion of the FT while the red dashed line shows the fit to the imaginary portion.

Table S3. Structural parameters for EXAFS fits of standard Rh foil (1 shell fit), and the model including Rh-Cu and Rh-Rh scattering paths for the RhCu/SiO₂ catalyst after H₂ reduction at 673 K.

Sample	Path	S_0^2	N	ΔE_0	R	$\sigma^2 \cdot 10^3$
Rh Foil	Rh-Rh	0.74 +/- 0.04	12	3.4 +/- 0.4	2.681 +/- 0.002	4.2 +/- 0.3
RhCu/SiO ₂ (H ₂ , 673 K)	Rh-Cu	0.74	9.0 +/- 1.1	1.8 +/- 1.7	2.57 +/- 0.01	6.6 +/- 1.4
	Rh-Rh		3.1 +/- 0.9		2.64 +/- 0.02	

Propane Dehydrogenation without Hydrogen in the Feed

Pt/Al₂O₃ catalysts deactivated quickly under non-oxidative propane dehydrogenation conditions (when no H₂ is co-fed), as shown by the red trace in Fig. S14 (68). In contrast, an initial induction period was observed for the RhCu/SiO₂ SAA, followed by a gradual decrease of the catalytic activity, which was significantly less rapid than for Pt/Al₂O₃ as shown by the black line in Fig. S14. The RhCu/SiO₂ SAA catalyst exhibited not only higher propylene activity per mol of active metal under these conditions but also had a much higher resistance to coking than Pt/Al₂O₃.

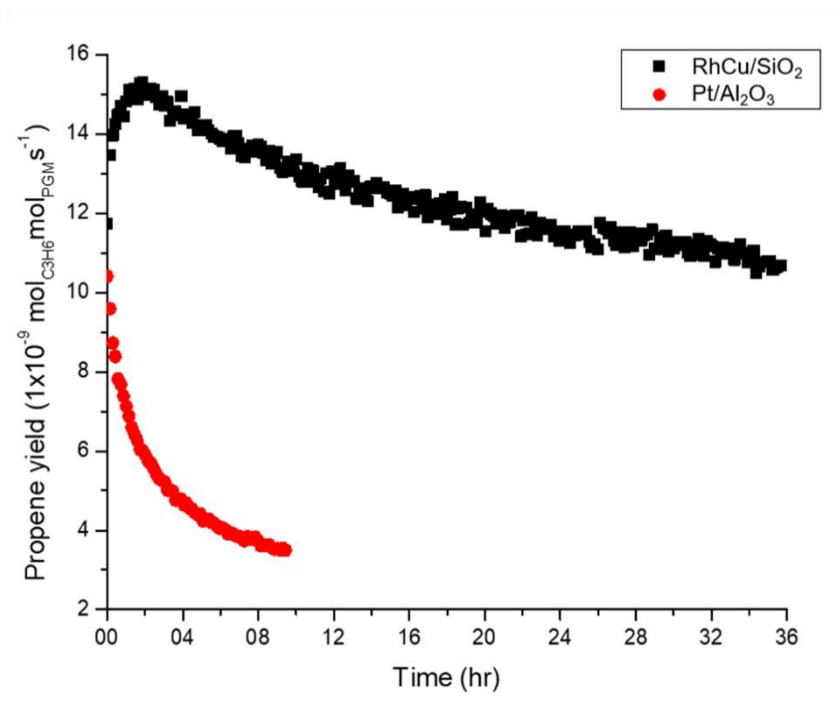


Fig. S14. Propene formation rate under the non-oxidative propane dehydrogenation reaction on RhCu/SiO₂ SAA and Pt/Al₂O₃ catalysts. Gas composition: 1.4 kPa propane, 90 mL/min, 10 mg of catalyst, 623 K.

Propene Selectivity with Hydrogen in the Feed

Selectivity to propene during the stability test in the presence of hydrogen (main text Fig. 3A inset) was monitored for the Pt/Al₂O₃ and RhCu/SiO₂ SAA catalysts and is shown in Fig. S15. No trace of methane, ethylene or other products was detected in the reactor outlet for RhCu/SiO₂ SAAs when operating at 623 K for more than 50 hours on stream putting the propene selectivity at 100%. In contrast, Pt/Al₂O₃ samples showed a considerably lower selectivity to propene (~65%), which despite increasing gradually, remained ~80% for the duration of the stability test (14 hours). The gradual increase is explained by the poisoning of the over-active and unselective sites by coke, leading to reduced reactivity and increased selectivity (69, 70).

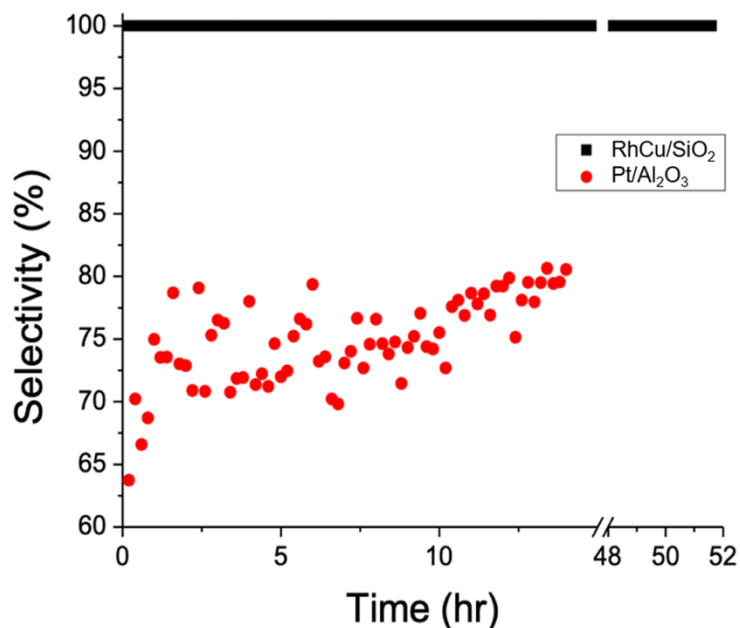


Fig. S15. Propene selectivity in the non-oxidative propane dehydrogenation reaction on RhCu/SiO₂ SAA and Pt/Al₂O₃ catalysts at 623 K. Gas composition: 1.4 kPa propane, 0.7kPa hydrogen, 90 mL/min.

Thermogravimetric Analysis

Pt/Al₂O₃ and RhCu/SiO₂ samples were exposed to a propane:H₂ mixture for more than 20 hours on stream at 773 K. The same amount of active metal was used for the Pt/Al₂O₃ and RhCu/SiO₂ catalysts and the residence time was varied such that ~30% equilibrium conversion was achieved for both catalysts. For Cu/SiO₂, excess catalyst was used to achieve initial reaction rates comparable to the other two catalysts. Two Pt/SiO₂ samples with different Pt loadings (0.5 wt.% and 0.1 wt.%) were also tested in order to provide a more direct comparison between the pure Pt and RhCu SAA catalysts on the same silica support, because alumina can enhance coke deposition during propane dehydrogenation (71). The results from these catalytic tests at reference conditions are shown in Table S4.

The thermogravimetric analysis (TGA) measurements themselves were performed on a TA instruments Q500 TGA. The samples were first pretreated under nitrogen flow (50 cc/min) up to 773 K and subsequently cooled to room temperature. The gas inlet was changed to O₂ (1% in He, 50 cc/min total flow) and the temperature was ramped up to 973 K (10 K/min) and kept there for 1 hr. Clear evidence for coke formation on Pt/Al₂O₃ was observed, while RhCu/SiO₂ SAA catalysts showed much lower coke formation, similar to that of the Cu/SiO₂ samples. The Pt/SiO₂ samples showed slightly lower coke deposition than Pt/Al₂O₃, which is consistent with the tendency of the strong Lewis acid sites present on alumina to enhance coke deposition.

Table S4. Results of thermogravimetric analysis on used Cu/SiO₂, RhCu/SiO₂ SAA, Pt/Al₂O₃, and Pt/SiO₂ (both 0.1 and 0.5 wt.%) catalysts.

Catalyst	mg C / g catalyst
Cu/SiO ₂	70
RhCu/SiO ₂ SAA	69
Pt/SiO ₂ (0.5 wt.%)	272
Pt/SiO ₂ (0.1 wt. %)	243
Pt/Al ₂ O ₃	412

Propane DFT

Free energies of gas phase species were calculated at a temperature T of 500 K and gas pressures of 1 kPa (C_3H_8 , H_2) and 0.01 Pa (C_3H_6) respectively in the ideal-gas limit assuming all spatial degrees of freedom are independent and separable into translational, rotational and vibrational degrees of freedom using the IdealGasThermo class implemented in atomic simulation environment (ASE). Free energy corrections of adsorbed species were calculated in the harmonic limit using the HarmonicThermo class in ASE (72). In the harmonic limit, all degrees of freedom are treated harmonically and correspond to the number of vibrational frequencies ν_i of the adsorbate ($3 \times n$). For transition states the imaginary frequency mode, which corresponds to the reaction coordinate, were not included and the number of degrees of freedom is $(3 \times n) - 1$. The free energy of adsorbates can be calculated from the harmonic vibrational energies ν_i according to the following formulas.

$$F = U - T \times S$$

$$U = E_{DFT} + E_{ZPE} + C_{v_{\text{harm}}}(0 \rightarrow T)$$

$$\text{with } E_{ZPE} = \sum_i 0.5 \nu_i, C_{v_{\text{harm}}}(0 \rightarrow T) = \sum_i \frac{\nu_i}{e^{\frac{\nu_i}{kT}} - 1},$$

$$\text{and } S = \sum_i \left[\frac{\frac{\nu_i}{kT}}{e^{\frac{\nu_i}{kT}} - 1} - \ln \left(1 - e^{-\frac{\nu_i}{kT}} \right) \right]$$

To compare the performance of the RhCu SAA to that of pure Cu, Pt and Rh, we calculated a free energy diagram for propane dehydrogenation to propene over Pt(111) and Rh(111). This is shown in Fig. S16, S17, and Table S5.

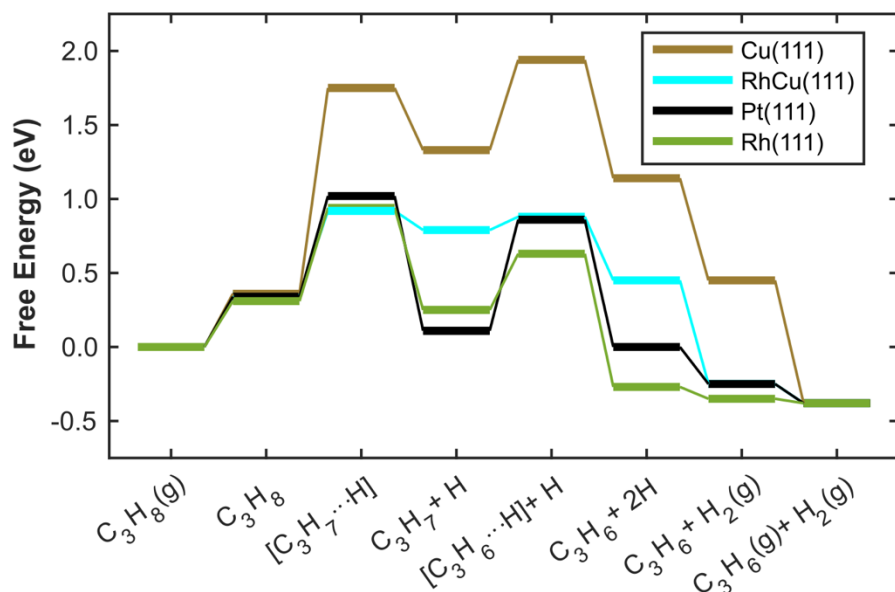


Fig. S16. Free energy diagrams for the non-oxidative dehydrogenation of propane on the RhCu(111) SAA, Cu(111), Pt(111) and Rh(111) surfaces. Free energies are calculated at 500 K and partial pressures of 1 kPa for C_3H_8 and H_2 , and 0.01 Pa for C_3H_6 . The energies are referenced with respect to the clean slabs, $C_3H_8(g)$ and $H_2(g)$. In the case of RhCu, H refers to an H atom adsorbed on the Cu host metal.

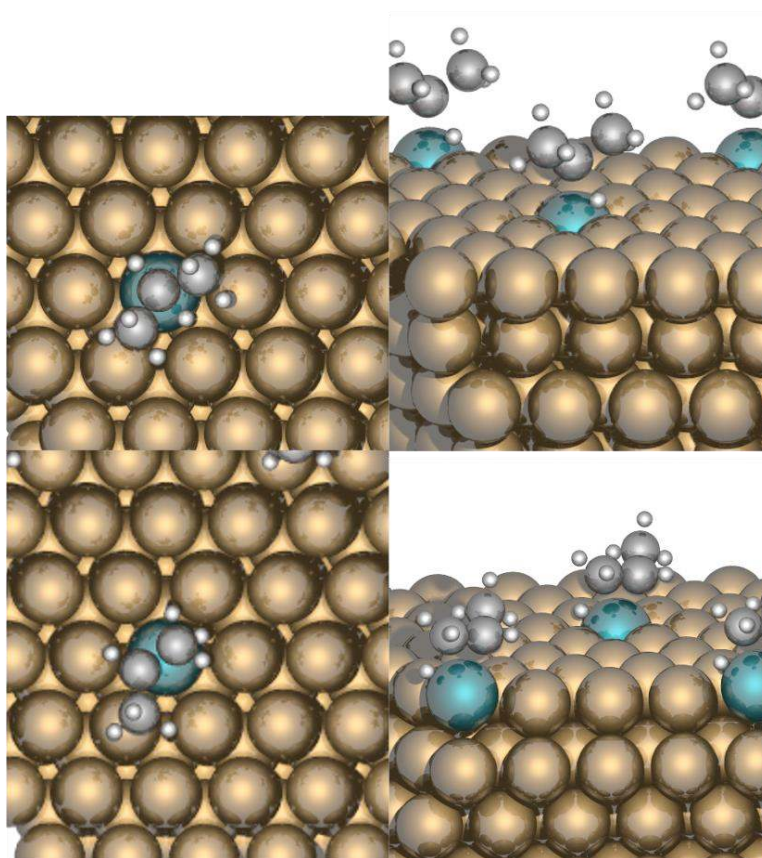


Fig. S17. Transition state structures for propane dehydrogenation on RhCu(111) SAAs. Top view (left) and side view (right) of C_3H_7-H (first dehydrogenation, upper panel) and C_3H_6-H (second dehydrogenation, lower panel).

Table S5. Free energies of intermediates and transition states for propane dehydrogenation as plotted in Fig. 3B and S16, respectively. Energies are given at 500 K and gas pressures of 1 kPa (each C_3H_8 and H_2) and 0.01 Pa (C_3H_6) respectively. All energies are given in eV. For the RhCu(111) SAA, the H adsorption energy is taken as adsorption on Cu host.

C_3H_8 (g)	0			
H_2 (g)	0			
C_3H_6 (g)	-0.38			
	RhCu(111)	Cu(111)	Pt(111)	Rh(111)
C_3H_8	0.35	0.36	0.34	0.31
C_3H_7-H (TS)	0.92	1.75	1.02	0.94
$C_3H_7 + H$	0.79	1.33	0.11	0.25
C_3H_6-H (TS) + H	0.88	1.94	0.86	0.63
$C_3H_6 + 2 H$	0.45	1.14	0.00	-0.27
$C_3H_6 + H_2(g)$	-0.25	0.45	-0.25	-0.35
C_3H_6 (g) + $H_2(g)$	-0.38			

Apparent Activation Energy Measurements

Measurements of the apparent activation energy for the non-oxidative propane dehydrogenation to propene on RhCu/SiO₂ SAAs were performed both in the presence and in the absence of H₂ in the feed, as shown in Fig. S18. In both cases, an apparent activation energy of ~0.7 eV was measured.

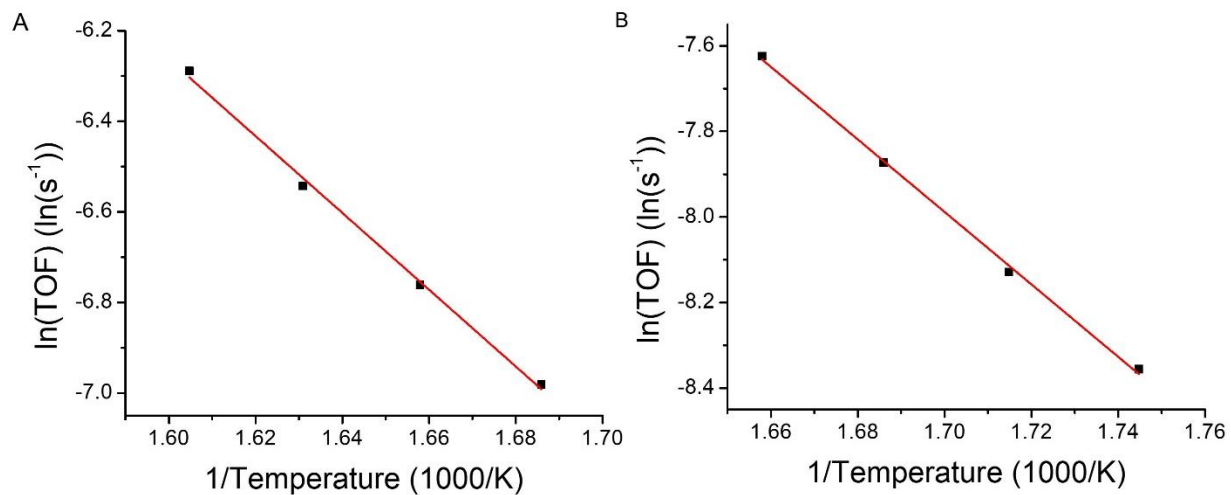


Fig. S18. Arrhenius plot for RhCu/SiO₂ in the presence and absence of hydrogen. (A) With hydrogen: C₃H₈:H₂ (2:1), 1.4 kPa C₃H₈ 100 cc/min. (B) Without hydrogen: 1.4 kPa C₃H₈ 100 cc/min.

Reactor Tests at 773 K

Reactor tests were also performed at elevated temperatures to compare the RhCu SAA catalyst performance to Pt/Al₂O₃. It should be noted that both catalysts deactivate under these conditions, but for different reasons. Pt/Al₂O₃ deactivates due to coke formation (see thermogravimetric analysis section above), while RhCu/SiO₂ SAAs undergo host particle sintering (27, 73). Regardless, the initial specific activity of RhCu/SiO₂ is higher than that of monometallic Pt/Al₂O₃ and Pt/SiO₂ on a per mol of active metal basis, as shown in Table S6. To provide context, a comparison to other catalysts reported in the literature is given.

Table S6. Comparison of the catalytic performance of RhCu/SiO₂ SAA to Pt/Al₂O₃ and Pt/SiO₂ tested at 773 K as well as to other catalysts reported in the literature for the non-oxidative propane dehydrogenation reaction.

Catalyst	Temperature (K)	WHSV (h ⁻¹)	Reactor Feed C ₃ H ₈ :H ₂ :Inert (%)	Initial Specific Activity (mol _{C₃H₆} mol ⁻¹ _{PGM} s ⁻¹)	Ref.
RhCu/SiO ₂ SAA	773	12	1.4:0.7:97.9	0.379	This work
Pt/Al ₂ O ₃ 0.5 wt.%	773	12	1.4:0.7:97.9	0.261	This work
Pt/SiO ₂ 0.5 wt.%	773	12	1.4:0.7:97.9	0.193	This work
Pt/SiO ₂ 0.1 wt.%	773	12	1.4:0.7:97.9	0.231	This Work
Pt/Al ₂ O ₃ 0.1 wt.%	793	4	16:16:68	0.2	(28)
PtCu/Al ₂ O ₃	793	4	16:16:68	0.41	(28)
PtSn/MgAl ₂ O ₄	823	36.6	50:50:0	0.497	(74)
PtCu/MgAl ₂ O ₄	853	6.8	47.5:47.5:5	0.188	(75)
PtSn/MgAl ₂ O ₄	853	2.4	10:10:80	0.34	(76)
PtFe/SBA-15	873	3.43	26:24:50	0.162	(77)
PtSn/Al ₂ O ₃	793	3.5	30:0:70	0.109	(78)
PtGa/Al ₂ O ₃	848	5.9	10:0:90	0.165	(79)
PtZn/SiO ₂	823	32	20:0:80	0.43	(80)
PtZn/NaY	828	2.6	100:0:0	0.145	(81)
Rh ₁ /ZrO ₂	823	1	40:0:60	0.38	(82)

References

1. F. Besenbacher, I. Chorkendorff, B. S. Clausen, B. Hammer, A. M. Molenbroek, J. K. Nørskov, I. Stensgaard, Design of a surface alloy catalyst for steam reforming. *Science* **279**, 1913–1915 (1998).
2. S. Alayoglu, A. U. Nilekar, M. Mavrikakis, B. Eichhorn, Ru-Pt core-shell nanoparticles for preferential oxidation of carbon monoxide in hydrogen. *Nat. Mater.* **7**, 333–338 (2008).
3. M. A. Gleeson, L. B. F. Juurlink, Site-specific dissociation on Pt. *Science* **157**, 155–157 (2019).
4. F. Tao, M. E. Grass, Y. Zhang, D. R. Butcher, J. R. Renzas, Z. Liu, J. Y. Chung, B. S. Mun, M. Salmeron, G. A. Somorjai, Reaction-driven restructuring of Rh-Pd and Pt-Pd core shell nanoparticles. *Science* **322**, 932–935 (2008).
5. B. Qiao, A. Wang, X. Yang, L. F. Allard, Z. Jiang, Y. Cui, J. Liu, J. Li, T. Zhang, Single-atom catalysis of CO oxidation using Pt₁/FeO_x. *Nat. Chem.* **3**, 634–641 (2011).
6. B. C. Gates, M. Flytzani-Stephanopoulos, D. A. Dixon, A. Katz, Atomically dispersed supported metal catalysts: Perspectives and suggestions for future research. *Catal. Sci. Technol.* **7**, 4259–4275 (2017).
7. J. Hulva, M. Meier, R. Bliem, Z. Jakub, F. Kraushofer, M. Schmid, U. Diebold, C. Franchini, G. S. Parkinson, Unraveling CO adsorption on model single-atom catalysts. *Science* **379**, 375–379 (2021).
8. L. DeRita, J. Resasco, S. Dai, A. Boubnov, H. V. Thang, A. S. Hoffman, I. Ro, G. W. Graham, S. R. Bare, G. Pacchioni, X. Pan, P. Christopher, Structural evolution of atomically dispersed Pt catalysts dictates reactivity. *Nat. Mater.* **18**, 746–751 (2019).
9. G. Kyriakou, M. B. Boucher, A. D. Jewell, E. A. Lewis, T. J. Lawton, A. E. Baber, H. L. Tierney, M. Flytzani-Stephanopoulos, E. C. H. Sykes, Isolated metal atom geometries as a strategy for selective heterogeneous hydrogenations. *Science* **335**, 1209–1212 (2012).
10. R. T. Hannagan, G. Giannakakis, M. Flytzani-Stephanopoulos, E. C. H. Sykes, Single-atom alloy catalysis. *Chem. Rev.* **120**, 12044–12088 (2020).
11. M. T. Darby, M. Stamatakis, A. Michaelides, E. C. H. Sykes, Lonely atoms with special gifts: Breaking linear scaling relationships in heterogeneous catalysis with single-atom alloys. *J. Phys. Chem. Lett.* **9**, 5636–5646 (2018).
12. G. Giannakakis, M. Flytzani-Stephanopoulos, E. C. H. Sykes, Single-atom alloys as a reductionist approach to the rational design of heterogeneous catalysts. *Acc. Chem. Res.* **52**, 237–247 (2019).
13. M. T. Darby, R. Réocreux, E. C. H. Sykes, A. Michaelides, M. Stamatakis, Elucidating the stability and reactivity of surface intermediates on single-atom alloy catalysts. *ACS Catal.* **8**, 5038–5050 (2018).
14. National Academies of Science, Engineering, and Medicine, *The changing landscape of hydrocarbon feedstocks for chemical production: Implications for catalysis: Proceedings of a workshop* (The National Academy of Science, Washington, DC, 2016).

15. D. Gerceker, A. H. Motagamwala, K. R. Rivera-Dones, J. B. Miller, G. W. Huber, M. Mavrikakis, J. A. Dumesic, methane conversion to ethylene and aromatics on PtSn catalysts. *ACS Catal.* **7**, 2088–2100 (2017).
16. M. T. Darby, E. C. H. Sykes, A. Michaelides, M. Stamatakis, Carbon monoxide poisoning resistance and structural stability of single atom alloys. *Top. Catal.* **61**, 428–438 (2018).
17. V. Fung, G. Hu, B. Sumpter, Electronic band contraction induced low temperature methane activation on metal alloys. *J. Mater. Chem. A* **8**, 6057–6066 (2020).
18. J. H. Sinfelt, D. J. C. Yates, Catalytic hydrogenolysis of ethane over the noble metals of Group VIII. *J. Catal.* **8**, 82–90 (1967).
19. R. T. Hannagan, D. A. Patel, L. A. Cramer, A. C. Schilling, P. T. P. Ryan, A. M. Larson, V. Çınar, Y. Wang, T. A. Balema, E. C. H. Sykes, Combining STM, RAIRS and TPD to decipher the dispersion and interactions between active sites in RhCu single-atom alloys. *ChemCatChem.* **12**, 488–493 (2019).
20. C. Chao-Ming, B. E. Bent, Methyl radical adsorption on Cu(111): Bonding, reactivity, and the effect of coadsorbed iodine. *Surf. Sci.* **279**, 79–88 (1992).
21. M. Pascal, C. L. A. Lamont, M. Kittel, J. T. Hoeft, L. Constant, M. Polcik, A. M. Bradshaw, R. L. Toomes, D. P. Woodruff, Methyl on Cu(1 1 1) - Structural determination including influence of co-adsorbed iodine. *Surf. Sci.* **512**, 173–184 (2002).
22. M. D. Marcinkowski, M. T. Darby, J. Liu, J. M. Wimble, F. R. Lucci, S. Lee, A. Michaelides, M. Flytzani-Stephanopoulos, M. Stamatakis, E. C. H. Sykes, Pt/Cu single-atom alloys as coke-resistant catalysts for efficient C-H activation. *Nat. Chem.* **10**, 325–332 (2018).
23. S. Gonzalez, C. Sousa, F. Illas, Features and catalytic properties of RhCu: A review. *Int. J. Mod. Phys. B* **24**, 5128–5138 (2010).
24. J. A. Anderson, C. H. Rochester, Z. Wang, IR study of CO adsorption on Cu-Rh/SiO₂ catalysts, coked by reaction with methane. *J. Mol. Catal. A Chem.* **139**, 285–303 (1999).
25. J. J. H. B. Sattler, J. Ruiz-Martinez, E. Santillan-Jimenez, B. M. Weckhuysen, Catalytic dehydrogenation of light alkanes on metals and metal oxides. *Chem. Rev.* **114**, 10613–10653 (2014).
26. N. Raman, S. Maisel, M. Grabau, N. Taccardi, J. Debuschewitz, M. Wolf, H. Wittkämper, T. Bauer, M. Wu, M. Haumann, C. Papp, A. Görling, E. Spiecker, J. Libuda, H. P. Steinrück, P. Wasserscheid, Highly effective propane dehydrogenation using Ga-Rh supported catalytically active liquid metal solutions. *ACS Catal.* **9**, 9499–9507 (2019).
27. M. V. Twigg, M. S. Spencer, Deactivation of copper metal catalysts for methanol decomposition, methanol steam reforming and methanol synthesis. *Top. Catal.* **22**, 191–203 (2003).
28. G. Sun, Z. J. Zhao, R. Mu, S. Zha, L. Li, S. Chen, K. Zang, J. Luo, Z. Li, S. C. Purdy, A. J. Kropf, J. T. Miller, L. Zeng, J. Gong, Breaking the scaling relationship via thermally stable Pt/Cu single atom alloys for catalytic dehydrogenation. *Nat. Commun.* **9**, 4454 (2018).
29. B. J. O’Neill, D. Jackson, A. J. Crisci, C. A. Farberow, J. Lu, P. J. Dietrich, T. Li, F. H. Ribeiro, J. T. Miller, R. Winans, J. W. Elam, J. Greeley, M. Mavrikakis, S. L. Scott, T. F. Kuech, J. A.

- Dumesic, Stabilization of copper catalysts for liquid phase reactions by Atomic Layer Deposition. *Angew. Chemie.* **125**, 14053–14057 (2013).
30. G. Kresse, J. Hafner, Ab initio molecular dynamics for liquid metals. *Phys. Rev. B* **47**, 558–561 (1993).
 31. G. Kresse, J. Furthmüller, Efficient iterative schemes for ab initio total-energy calculations using a plane-wave basis set. *Phys. Rev. B* **54**, 11169–11186 (1996).
 32. G. Kresse, J. Furthmüller, Efficiency of ab-initio total energy calculations for metals and semiconductors using a plane-wave basis set. *Comput. Mater. Sci.* **6**, 15–50 (1996).
 33. M. Dion, H. Rydberg, E. Schröder, D. C. Langreth, B. I. Lundqvist, Van der Waals density functional for general geometries. *Phys. Rev. Lett.* **92**, 22–25 (2004).
 34. J. Klimeš, D. R. Bowler, A. Michaelides, Chemical accuracy for the van der Waals density functional. *J. Phys. Condens. Matter.* **22**, 022201 (2010).
 35. J. Klimeš, D. R. Bowler, A. Michaelides, Van der Waals density functionals applied to solids. *Phys. Rev. B* **83**, 195131 (2011).
 36. J. Klimeš, A. Michaelides, Perspective: Advances and challenges in treating van der Waals dispersion forces in density functional theory. *J. Chem. Phys.* **137**, 120901 (2012).
 37. P. E. Blöchl, Projector augmented-wave method. *Phys. Rev. B* **50**, 17953–17979 (1994).
 38. G. Kresse, D. Joubert, From ultrasoft pseudopotentials to the projector augmented-wave method. *Phys. Rev. B* **59**, 1758–1775 (1999).
 39. H. J. Monkhorst, J. D. Pack, Special points for Brillouin zone integrations. *J. Mater. Chem. A* **13**, 5188–5192 (1976).
 40. D. Sheppard, R. Terrell, G. Henkelman, Optimization methods for finding minimum energy paths. *J. Chem. Phys.* **128**, 134106 (2008).
 41. G. Henkelman, B. P. Uberuaga, H. Jónsson, Climbing image nudged elastic band method for finding saddle points and minimum energy paths. *J. Chem. Phys.* **113**, 9901–9904 (2000).
 42. A. Heyden, A. T. Bell, F. J. Keil, Efficient methods for finding transition states in chemical reactions: Comparison of improved dimer method and partitioned rational function optimization method. *J. Chem. Phys.* **123**, 224101 (2005).
 43. G. Henkelman, H. Jónsson, A dimer method for finding saddle points on high dimensional potential surfaces using only first derivatives. *J. Chem. Phys.* **111**, 7010–7022 (1999).
 44. K. G. Papanikolaou, M. T. Darby, M. Stamatakis, CO-induced aggregation and segregation of highly dilute alloys: A Density Functional Theory Study. *J. Phys. Chem. C* **123**, 9128–9138 (2019).
 45. X. Wei, J. Liu, G. J. Xia, J. Deng, P. Sun, J. J. Chruma, W. Wu, C. Yang, Y. G. Wang, Z. Huang, Enantioselective photoinduced cyclodimerization of a prochiral anthracene derivative adsorbed on helical metal nanostructures. *Nat. Chem.* **12**, 551–559 (2020).
 46. E. Clementi, D. L. Raimondi, W. P. Reinhardt, Atomic screening constants from SCF functions. II. Atoms with 37 to 86 electrons. *J. Chem. Phys.* **47**, 1300–1307 (1967).

47. Y. Wang, K. G. Papanikolaou, R. Hannagan, D. Patel, T. Balema, L. Cramer, P. Kress, M. Stamatakis, E. C. H. Sykes, Surface facet dependence of competing alloying mechanisms. *J. Chem. Phys.* **153**, 244702 (2020).
48. D. O. Bellisario, J. W. Han, H. L. Tierney, A. E. Baber, D. S. Sholl, E. C. H. Sykes, Importance of kinetics in surface alloying: A comparison of the diffusion pathways of Pd and Ag atoms on Cu(111). *J. Phys. Chem. C* **113**, 12863–12869 (2009).
49. P. Varga, M. Schmid, Chemical discrimination on atomic level by STM. *Appl. Surf. Sci.* **141**, 287–293 (1999).
50. J. Tersoff, D. R. Hamann, Theory of the scanning tunneling microscope. *Phys. Rev. B* **31**, 805–813 (1985).
51. D. E. P. Vanpoucke, G. Brocks, Formation of Pt-induced Ge atomic nanowires on Pt/Fe(001): A density functional theory study. *Phys. Rev. B* **77**, 241308(R) (2008).
52. F. Solymosi, G. Klivényi, HREELS study of CH₃I and CH₃ adsorbed on Rh(111) surface. *J. Electron Spectros. Relat. Phenomena.* **64–65**, 499–506 (1993).
53. J. Lin, B. E. Bent, Iodomethane dissociation on Cu(111): Bonding and chemistry of adsorbed methyl groups. *J. Vac. Sci. Technol. A* **10**, 2202–2209 (1992).
54. Z. Ma, F. Zaera, Organic chemistry on solid surfaces. *Surf. Sci. Rep.* **61**, 229–281 (2006).
55. F. R. Lucci, J. Liu, M. D. Marcinkowski, M. Yang, L. F. Allard, M. Flytzani-Stephanopoulos, E. C. H. Sykes, Selective hydrogenation of 1,3-butadiene on platinum-copper alloys at the single-atom limit. *Nat. Commun.* **6**, 8550 (2015).
56. M. B. Boucher, B. Zugic, G. Cladaras, J. Kammert, M. D. Marcinkowski, T. J. Lawton, E. C. H. Sykes, M. Flytzani-Stephanopoulos, Single atom alloy surface analogs in Pd_{0.18}Cu₁₅ nanoparticles for selective hydrogenation reactions. *Phys. Chem. Chem. Phys.* **15**, 12187–12196 (2013).
57. G. Giannakakis, A. Trimpalis, J. Shan, Z. Qi, S. Cao, J. Liu, J. Ye, J. Biener, M. Flytzani-Stephanopoulos, NiAu single atom alloys for the non-oxidative dehydrogenation of ethanol to acetaldehyde and hydrogen. *Top. Catal.* **61**, 475–486 (2018).
58. J. W. Harris, J. A. Herron, J. F. DeWilde, A. Bhan, Molecular characteristics governing chlorine deposition and removal on promoted Ag catalysts during ethylene epoxidation. *J. Catal.* **377**, 378–388 (2019).
59. N. D. Subramanian, C. S. S. R. Kumar, K. Watanabe, P. Fischer, R. Tanaka, J. J. Spivey, A DRIFTS study of CO adsorption and hydrogenation on Cu-based core-shell nanoparticles. *Catal. Sci. Technol.* **2**, 621–631 (2012).
60. F. M. T. Mendes, M. Schmal, The cyclohexanol dehydrogenation on Rh-Cu/Al₂O₃ catalysts part 1. Characterization of the catalyst. *Appl. Catal. A Gen.* **151**, 393–408 (1997).
61. J. C. Matsubu, V. N. Yang, P. Christopher, Isolated metal active site concentration and stability control catalytic CO₂ reduction selectivity. *J. Am. Chem. Soc.* **137**, 3076–3084 (2015).
62. A. C. Yang, C. W. Garland, Infrared studies of carbon monoxide chemisorbed on rhodium. *J. Phys. Chem.* **61**, 1504–1512 (1957).

63. J. T. Yates, T. M. Duncan, R. W. Vaughan, Infrared spectroscopic study of activated surface processes: CO chemisorption on supported Rh. *J. Chem. Phys.* **71**, 3908–3915 (1979).
64. J. Resasco, P. Christopher, Atomically dispersed Pt-group catalysts: Reactivity, uniformity, structural evolution, and paths to increased functionality. *J. Phys. Chem. Lett.* **11**, 10114–10123 (2020).
65. B. Ravel, M. Newville, ATHENA, ARTEMIS, HEPHAESTUS: Data analysis for X-ray absorption spectroscopy using IFEFFIT. *J. Synchrotron Radiat.* **12**, 537–541 (2005).
66. J. J. Rehr, R. C. Albers, S. I. Zabinsky, High-order multiple-scattering calculations of x-ray-absorption fine structure. *Phys. Rev. Lett.* **69**, 3397–3400 (1992).
67. L. Zhou, J. M. P. Martirez, J. Finzel, C. Zhang, D. F. Swearer, S. Tian, H. Robotjazi, M. Lou, L. Dong, L. Henderson, P. Christopher, E. A. Carter, P. Nordlander, N. J. Halas, Light-driven methane dry reforming with single atomic site antenna-reactor plasmonic photocatalysts. *Nat. Energy.* **5**, 61–70 (2020).
68. A. Iglesias-Juez, A. M. Beale, K. Maaijen, T. C. Weng, P. Glatzel, B. M. Weckhuysen, A combined in situ time-resolved UV-Vis, Raman and high-energy resolution X-ray absorption spectroscopy study on the deactivation behavior of Pt and PtSn propane dehydrogenation catalysts under industrial reaction conditions. *J. Catal.* **276**, 268–279 (2010).
69. W. Zhang, H. Wang, J. Jiang, Z. Sui, Y. Zhu, D. Chen, X. Zhou, Size dependence of Pt catalysts for propane dehydrogenation: From atomically dispersed to nanoparticles. *ACS Catal.* **10**, 12932–12942 (2020).
70. J. Zhu, M. L. Yang, Y. Yu, Y. A. Zhu, Z. J. Sui, X. G. Zhou, A. Holmen, D. Chen, Size-dependent reaction mechanism and kinetics for propane dehydrogenation over Pt catalysts. *ACS Catal.* **5**, 6310–6319 (2015).
71. E. J. Jang, J. Lee, H. Y. Jeong, J. H. Kwak, Controlling the acid-base properties of alumina for stable PtSn-based propane dehydrogenation catalysts. *Appl. Catal. A Gen.* **572**, 1–8 (2019).
72. A. Hjorth Larsen, J. Jørgen Mortensen, J. Blomqvist, I. E. Castelli, R. Christensen, M. Dułak, J. Friis, M. N. Groves, B. Hammer, C. Hargus, E. D. Hermes, P. C. Jennings, P. Bjerre Jensen, J. Kermode, J. R. Kitchin, E. Leonhard Kolsbjerg, J. Kubal, K. Kaasbjerg, S. Lysgaard, J. Bergmann Maronsson, T. Maxson, T. Olsen, L. Pastewka, A. Peterson, C. Rostgaard, J. Schiøtz, O. Schütt, M. Strange, K. S. Thygesen, T. Vegge, L. Vilhelmsen, M. Walter, Z. Zeng, K. W. Jacobsen, The atomic simulation environment - A Python library for working with atoms. *J. Phys. Condens. Matter.* **29**, 273002 (2017).
73. J. Shan, N. Janvelyan, H. Li, J. Liu, T. M. Egle, J. Ye, M. M. Biener, J. Biener, C. M. Friend, M. Flytzani-Stephanopoulos, Selective non-oxidative dehydrogenation of ethanol to acetaldehyde and hydrogen on highly dilute NiCu alloys. *Appl. Catal. B Environ.* **205**, 541–550 (2017).
74. J. Salmones, J. A. Wang, J. A. Galicia, G. Aguilar-Rios, H₂ reduction behaviors and catalytic performance of bimetallic tin-modified platinum catalysts for propane dehydrogenation. *J. Mol. Catal. A Chem.* **184**, 203–213 (2002).

75. G. Q. Ren, G. X. Pei, Y. J. Ren, K. P. Liu, Z. Q. Chen, J. Y. Yang, Y. Su, X. Y. Liu, W. Z. Li, T. Zhang, Effect of group IB metals on the dehydrogenation of propane to propylene over anti-sintering Pt/MgAl₂O₄. *J. Catal.* **366**, 115–126 (2018).
76. H. Zhu, D. H. Anjum, Q. Wang, E. Abou-Hamad, L. Emsley, H. Dong, P. Laveille, L. Li, A. K. Samal, J. M. Basset, Sn surface-enriched Pt-Sn bimetallic nanoparticles as a selective and stable catalyst for propane dehydrogenation. *J. Catal.* **320**, 52–62 (2014).
77. W. Cai, R. Mu, S. Zha, G. Sun, S. Chen, Z. J. Zhao, H. Li, H. Tian, Y. Tang, F. Tao, L. Zeng, J. Gong, Subsurface catalysis-mediated selectivity of dehydrogenation reaction. *Sci. Adv.* **4**, 5418 (2018).
78. O. A. Bariás, A. Holmen, E. A. Blekkan, Propane dehydrogenation over supported Pt and Pt-Sn catalysts: Catalyst preparation, characterization, and activity measurements. *J. Catal.* **158**, 1–12 (1996).
79. Y. Xu, J. Chen, X. Yuan, Y. Zhang, J. Yu, H. Liu, M. Cao, X. Fan, H. Lin, Q. Zhang, Sintering-resistant Pt on Ga₂O₃ rods for propane dehydrogenation: The morphology matters. *Ind. Eng. Chem. Res.* **57**, 13087–13093 (2018).
80. L. Rochlitz, K. Searles, J. Alfke, D. Zemlyanov, O. V. Safonova, C. Copéret, Silica-supported, narrowly distributed, subnanometric Pt-Zn particles from single sites with high propane dehydrogenation performance. *Chem. Sci.* **11**, 1549–1555 (2020).
81. P. L. De Cola, R. Gläser, J. Weitkamp, Non-oxidative propane dehydrogenation over Pt-Zn-containing zeolites. *Appl. Catal. A Gen.* **306**, 85–97 (2006).
82. Y. Zhang, Y. Zhang, Y. Zhao, T. Otroshchenko, A. Perechodjuk, V. A. Kondratenko, S. Bartling, U. Rodemerck, D. Linke, H. Jiao, G. Jiang, E. V. Kondratenko, Structure-activity-selectivity relationships in propane dehydrogenation over Rh/ZrO₂ catalysts. *ACS Catal.* **10**, 6377–6388 (2020).